

Inferring the oriented elastic tensor from surface wave observations: preliminary application across the western United States

Jiayi Xie,¹ Michael H. Ritzwoller,¹ S.J. Brownlee² and B.R. Hacker³

¹Center for Imaging the Earth's Interior, Department of Physics, University of Colorado Boulder, Boulder, CO 80309-0390, USA.

E-mail: jiayi.xie@colorado.edu

²Department of Geology, Wayne State University, Detroit, MI 48202, USA

³Department of Earth Science, UC Santa Barbara, CA 93106-9630, USA

Accepted 2015 February 2. Received 2015 January 23; in original form 2014 September 14

SUMMARY

Radial and azimuthal anisotropy in seismic wave speeds have long been observed using surface waves and are believed to be controlled by deformation within the Earth's crust and uppermost mantle. Although radial and azimuthal anisotropy reflect important aspects of anisotropic media, few studies have tried to interpret them jointly. We describe a method of inversion that interprets simultaneous observations of radial and azimuthal anisotropy under the assumption of a hexagonally symmetric elastic tensor with a tilted symmetry axis defined by dip and strike angles. We show that observations of radial anisotropy and the 2ψ component of azimuthal anisotropy for Rayleigh waves obtained using USArray data in the western United States can be fit well under this assumption. Our inferences occur within the framework of a Bayesian Monte Carlo inversion, which yields a posterior distribution that reflects both variances of and covariances between all model variables, and divide into theoretical and observational results. Principal theoretical results include the following: (1) There are two distinct groups of models (Group 1, Group 2) in the posterior distribution in which the strike angle of anisotropy in the crust (defined by the intersection of the foliation plane with Earth's surface) is approximately orthogonal between the two sets. (2) The Rayleigh wave fast axis directions are orthogonal to the strike angle in the geologically preferred group of models in which anisotropy is strongly non-elliptical. (3) The estimated dip angle may be interpreted in two ways: as a measure of the actual dip of the foliation of anisotropic material within the crust, or as a proxy for another non-geometric variable, most likely a measure of the deviation from hexagonal symmetry of the medium. The principal observational results include the following: (1) Inherent *S*-wave anisotropy (γ) is fairly homogeneous vertically across the crust, on average, and spatially across the western United States. (2) Averaging over the region of study and in depth, γ in the crust is approximately 4.1 ± 2 percent. γ in the crust is approximately the same in the two groups of models. (3) Dip angles in the two groups of models show similar spatial variability and display geological coherence. (4) Tilting the symmetry axis of an anisotropic medium produces apparent radial and apparent azimuthal anisotropies that are both smaller in amplitude than the inherent anisotropy of the medium, which means that most previous studies have probably underestimated the strength of anisotropy.

Key words: Surface waves and free oscillations; Seismic anisotropy; Seismic tomography; Crustal structure.

1 INTRODUCTION

The study of anisotropy using surface waves is primarily of interest to seismologists because surface waves provide a homogenous sampling of the Earth's crust and uppermost mantle over large areas. Robust inferences about anisotropy from surface waves are typically not restricted to small regions, allowing conclusions to

be drawn broadly over a variety of geologic and tectonic settings (e.g. Anderson & Regan 1983; Ekström & Dziewoński 1998; Gung *et al.* 2003; Smith *et al.* 2004; Kustowski *et al.* 2008; Nettles & Dziewoński 2008). Cross-correlations of ambient noise principally present relatively short and intermediate period surface waves for interpretation. Therefore, the introduction of ambient noise surface wave tomography has allowed for increasingly detailed information

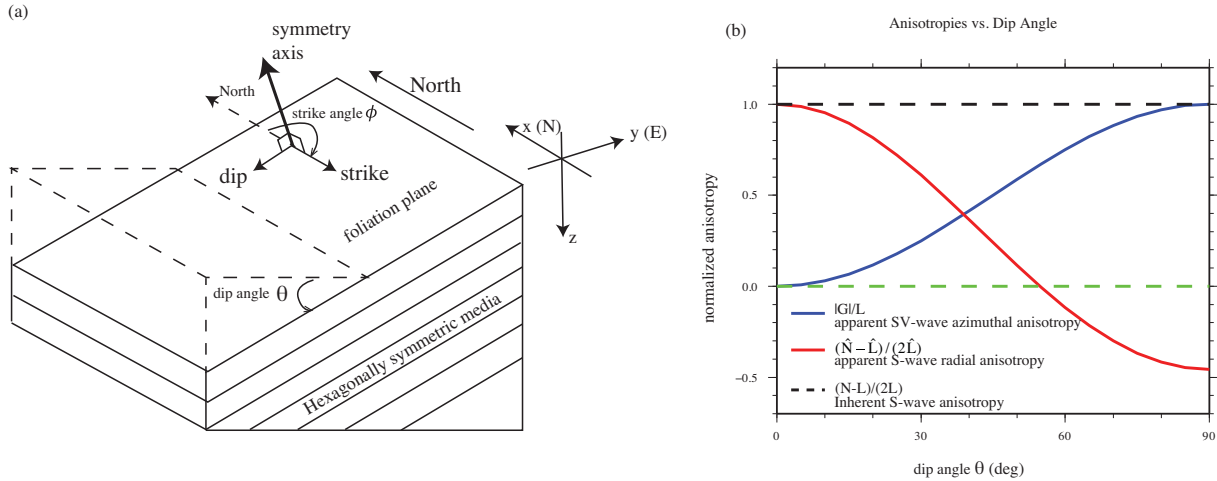


Figure 1. (a) Depiction of a tilted hexagonally symmetric medium with definitions of the foliation plane, symmetry axis, strike angle, and dip angle. (b) Illustrative computation of the variation of apparent S -wave radial ($\hat{\gamma}$, red curve) and SV-wave azimuthal (blue curve) anisotropy as a function of dip angle θ . All amplitudes are normalized by the amplitude of maximum inherent S -wave anisotropy, γ . These quantities are defined by eqs (9) and (11), and they are obtained by rotating a hexagonally symmetric elastic tensor based on the effective anisotropic medium theory (Montagner & Nataf 1986). This figure aims to summarize qualitatively the variation of anisotropy with dip angle. Details (e.g. the absolute amplitude, the zero-crossing angle, and the number of crossing angles) depend on the elastic tensor.

to be gained about the crust over broad regions (e.g. Shapiro *et al.* 2005; Yao *et al.* 2006; Bensen *et al.* 2009; Moschetti *et al.* 2010a; Ritzwoller *et al.* 2011; Yang *et al.* 2012; Ekström 2013), and information about anisotropy from ambient noise mainly concerns the crust (e.g. Huang *et al.* 2010; Moschetti *et al.* 2010b; Yao *et al.* 2010; Lin *et al.* 2011; Xie *et al.* 2013). In this paper, surface wave observations obtained from both ambient noise and earthquakes will be used, and the principal focus will be on the means to infer crustal anisotropy.

Studies of seismic anisotropy using surface waves primarily take two forms. In the first, azimuthally averaged (transversely isotropic) Rayleigh and Love wave traveltime (or dispersion) curves are studied to determine if they are consistent with an isotropic medium of propagation. If not, radial anisotropy (or polarization anisotropy) is introduced to the medium to resolve what is often called the ‘Rayleigh-Love discrepancy’ (e.g. Forsyth 1975; Dziewonski & Anderson 1981; Moschetti *et al.* 2010b; Xie *et al.* 2013). In the second form, the directional dependence of surface wave traveltimes is used to determine azimuthal anisotropy (e.g. Simons *et al.* 2002; Marone & Romanowicz 2007; Yao *et al.* 2010; Lin *et al.* 2011). In both cases, the anisotropy is typically interpreted to result from the mechanism of formation of the medium, either through (1) the crystallographic or lattice preferred orientation of anisotropic minerals (Christensen 1984; Ribe 1992) or (2) the anisotropic shape distribution of isotropic materials, such as laminated structure (Backus 1962; Kawakatsu *et al.* 2009) or fluid filled cracks (Anderson *et al.* 1974; Crampin 1984; Babuška 1991). Indeed, one of the principal motivations to study seismic anisotropy is to understand the deformation that a medium was subject to during its formation and evolution.

The anisotropic properties of an elastic medium and the anisotropy of seismic wave speeds both depend on the detailed constitution of the elastic tensor and on its orientation. With several notable exceptions (e.g. Montagner & Jobert 1988; Dziewonski & Anderson 1981) most studies of seismic anisotropy with surface waves model only the polarization or azimuthal dependence of shear wave speeds and do not explicitly attempt to estimate the elastic tensor. Because, as we discuss below, the directional dependence

of surface waves may be ambiguously related to the deformation of the transport medium, in order to understand the anisotropy that seismic waves exhibit and its relationship to the deformation that causes it, it is important to seek information about the (depth-dependent) elastic tensor within the crust and mantle together with its orientation. We refer to the anisotropic properties of a medium as ‘inherent anisotropy’ when they are based on a measured (or inferred) elastic tensor with a known orientation. We use the term ‘inherent’ as opposed to ‘intrinsic’ anisotropy because the latter term often refers to anisotropy that results from a specific cause, namely, from crystal orientation (Wang *et al.* 2013; Thomsen & Anderson 2015). Therefore, we use the term inherent as more general than intrinsic or extrinsic anisotropy, but not directly in conflict with these terms (e.g. Wang *et al.* 2013). The term inherent may also be contrasted with ‘apparent’ anisotropy, which would be inferred from observational studies that have not explicitly estimated the elastic tensor and its orientation.

A useful starting point on which to base estimates of the elastic tensor is the simplifying assumption that the medium possesses hexagonal symmetry. Such a medium has one symmetry axis, and if the symmetry axis is either vertical or horizontal the elastic tensor can be represented with five independent elastic moduli. A hexagonally symmetric medium with a vertical symmetry axis (z -axis in Fig. 1) is referred to as a vertical transversely isotropic medium or VTI medium. Such a medium is defined by five depth-dependent elastic parameters (A , C , N , L , F or η), where A and C are compressional moduli and N and L are shear moduli. In this case, the 6×6 elastic modulus matrix, $C_{\alpha\beta}$, the Voigt simplification of the elastic tensor, can be written as the following symmetric matrix:

$${}^V C_{\alpha\beta} = \begin{bmatrix} A & A - 2N & F & 0 & 0 & 0 \\ A - 2N & A & F & 0 & 0 & 0 \\ F & F & C & 0 & 0 & 0 \\ 0 & 0 & 0 & L & 0 & 0 \\ 0 & 0 & 0 & 0 & L & 0 \\ 0 & 0 & 0 & 0 & 0 & N \end{bmatrix} \quad (1)$$

where $\eta = F/(A - 2L)$ and the superscript V stands for vertical. With a vertical symmetry axis, a hexagonally symmetric medium will produce no azimuthal variation in surface wave speeds mainly because the C_{44} and C_{55} matrix elements are identical. A hexagonally symmetric elastic tensor may display either slow or fast symmetry. In the slow symmetry case, $C < A$ and $L < N$, which is referred to as positive S -wave radial anisotropy and implies that Love waves are faster than predicted from an isotropic medium that fits Rayleigh wave speeds. Crustal rocks generally display slow symmetry and a finely layered medium also requires it (Thomsen & Anderson 2015; Tatham *et al.* 2008; Brownlee *et al.* 2011; Erdman *et al.* 2013). For the mantle, however, rocks abundant in olivine are sometimes considered hexagonally symmetric with a fast symmetry axis, because seismologists have assumed that the two slower olivine crystal axes scatter randomly perpendicular to the average fast axis (Park & Levin 2002). However, melt-rich layers embedded in a meltless mantle (Kawakatsu *et al.* 2009; Jaxybulatov *et al.* 2014) probably have a slow symmetry axis.

In contrast, if a hexagonally symmetric medium has a horizontal symmetry axis (x -axis in Fig. 1), it is referred to as a HTI medium (horizontal transversely isotropic) and the elastic modulus matrix has the following form:

$${}^H C_{\alpha\beta} = \begin{bmatrix} C & F & F & 0 & 0 & 0 \\ F & A & A - 2N & 0 & 0 & 0 \\ F & A - 2N & A & 0 & 0 & 0 \\ 0 & 0 & 0 & N & 0 & 0 \\ 0 & 0 & 0 & 0 & L & 0 \\ 0 & 0 & 0 & 0 & 0 & L \end{bmatrix}. \quad (2)$$

In this case, if N is larger than L ($C_{44} > C_{66}$) then there would be negative S -wave radial anisotropy, which is observed in the mantle beneath the mid-ocean ridges (e.g. Ekström & Dziewoński 1998; Zhou *et al.* 2006; Nettles & Dziewoński 2008) but is observed only rarely in the crust (e.g. Xie *et al.* 2013). Also, mainly because $C_{44} \neq C_{55}$, this elastic tensor would generate azimuthal variations in wave speeds.

Assumptions of either vertical or horizontal hexagonal symmetry are inconsistent with one another and cannot explain the widely observed co-existence of positive S -wave radial anisotropy along with azimuthal anisotropy (e.g. Huang *et al.* 2010; Yao *et al.* 2010; Yuan & Romanowicz 2010; Yuan *et al.* 2011; Xie *et al.* 2013; Burgos *et al.* 2014; Hacker *et al.* 2014), at least for the case of a slow symmetry axis. The purpose of this paper is to describe a method to interpret observations of radial and azimuthal anisotropy simultaneously under the assumption of a hexagonally symmetric elastic tensor with a tilted symmetry axis (Fig. 1a), as was first suggested by Montagner & Nataf (1988) and applied at a global scale across the Indian Ocean by Montagner & Jobert (1988). Such an assumption has been applied before to body wave observations (e.g. Okaya & McEvelly 2003) as well as studies of the effect of mode-coupling on surface waves (e.g. Yu & Park 1993).

The assumption of hexagonal symmetry is a starting point designed to reduce the number of free parameters that govern the anisotropic medium, which simplifies and accelerates the inverse problem. To describe the medium under this assumption at a given depth requires seven unknowns, the five moduli that govern the inherent characteristics of a hexagonally symmetric medium and two angles through which the elastic tensor is rotated: the dip and strike angles. There are, however, reasons to believe that crustal anisotropy, which is the primary focus of this paper, may display dominantly

hexagonal symmetry. For example, strongly laminated or foliated rocks are nearly hexagonal in symmetry (Okaya & McEvelly 2003) and lamination in the lower crust has been observed worldwide (Meissner *et al.* 2006). Also, the primary anisotropic mineral in the middle crust is probably mica (Weiss *et al.* 1999; Meissner *et al.* 2006), which displays approximate hexagonal symmetry. Therefore, if anisotropy derives from the CPO of anisotropic minerals, then mid-crustal anisotropy may be well approximated by an inherently hexagonally symmetric elastic tensor. However, as discussed later in the paper, amphiboles are also strongly anisotropic and may be the dominant anisotropic mineral in the lower crust, but are more orthorhombic than hexagonal in symmetry (Meissner *et al.* 2006; Tatham *et al.* 2008). If amphiboles are a significant source of anisotropy, then what we estimate by assuming hexagonal symmetry may not have direct geologic relevance, but may yet contain information about the lower-order symmetry of the real elastic tensor, and inferences that are derived should be cognizant of this.

Two further comments will conclude this discussion. First, Rayleigh and Love waves are strongly sensitive only to four (N , L , θ , ϕ , as described later) of the seven unknowns that define a rotated hexagonally symmetric elastic medium. Therefore, a straightforward inversion for the elastic tensor is impractical using surface wave data alone. For this reason we cast the inverse problem in terms of a Bayesian Monte Carlo approach in which we estimate a range of elastic tensors that agree with the data. This allows us to estimate uncertainties in all variables as well as the covariances or correlations between them as represented by the ‘posterior distribution’ at each location and depth. As discussed later, we find that certain elements of the elastic tensor are well determined, others are not, and the posterior distribution is bimodal in three important variables. Secondly, the assumption of hexagonal symmetry is actually not required for the method we present, but simplifies it significantly. We could have, for example, cast the inverse problem in terms of an untilted orthorhombic elastic tensor, but at the expense of introducing two additional free parameters.

Applications here are made using Rayleigh and Love wave dispersion maps from the western United States obtained using the Transportable Array (TA) stations from EarthScope USArray. We obtain isotropic Rayleigh wave phase speed maps from 8 to 40 s period from ambient noise data and from 24 to 90 s period from earthquake data. Isotropic Love wave maps are taken from ambient noise data from 10 to 25 s period and from earthquake data from 24 to 50 s period. These observations produce azimuthally isotropic Rayleigh and Love wave phase speed curves at each point on a $0.2^\circ \times 0.2^\circ$ grid across the study region. The 2ψ Rayleigh wave azimuthal anisotropy data are obtained from 10 to 40 s from ambient noise data and 24–60 s period from earthquake data, where ψ is the azimuth of propagation of the wave. No azimuthal anisotropy data from Love waves are used in this study. Love wave azimuthal variations are expected (and observed) to display dominantly 4ψ azimuthal variation, which is a much more difficult observation to make than the 2ψ azimuthal variation of Rayleigh waves.

In Section 2, we briefly describe the data we use and the observations from surface waves that serve as the input data for the inversion. In Section 3, we explain the theoretical background of the inversion, concentrating on the connections between surface wave observations and elastic constants. In Sections 4 and 5, the model parametrization and inversion are discussed. Finally, in Section 6, we present the inversion results and discuss possible physical implications of the estimated models.

2 SURFACE WAVE DATA

This paper is motivated by the need for a new inversion method, which is described in a later section that self-consistently interprets observations of radial and azimuthal anisotropy of surface waves. The method is applied here to surface wave data obtained in a region that encompasses the western United States and part of the central United States, where USArray stations operated between the years 2005 and 2010. We use continuous ambient noise data to measure Rayleigh and Love wave phase speeds between station-pairs and data from earthquakes with $M_w > 5.0$ to generate dispersion curves between event-station pairs. We follow the tomographic methods described by Lin *et al.* (2009) and Lin & Ritzwoller (2011) known as eikonal and Helmholtz tomography to estimate phase velocity maps with uncertainties. Our region of study extends somewhat further eastward than these earlier studies, however, and we obtain Love wave dispersion maps in addition to Rayleigh wave maps.

At short periods, we use only ambient noise data and at very long periods only earthquake data, but there is an intermediate period range where ambient noise data and earthquake data are combined. The short period interval extends from 8 to 22 s period where we apply eikonal tomography to produce the Rayleigh wave dispersion maps (Lin *et al.* 2009) from ambient noise. The period band of overlap of ambient noise and earthquake measurements for Rayleigh waves is broad, ranging from 24 to 40 s period. Love wave measurements, however, only extend up to 25 s period for ambient noise so overlap between ambient noise and earthquake measurements occurs only at 25 s period. At longer periods (>40 s for Rayleigh waves, > 25 s for Love waves) earthquake data alone are used, with Rayleigh wave measurements extending to 90 s period and Love wave measurements to 50 s period. The signal-to-noise ratio is smaller at long periods for Love waves than for Rayleigh waves, which reduces the longest period that Love wave phase speed maps can be constructed. Following the recommendation of Lin & Ritzwoller (2011), we apply eikonal tomography up to 50 s period but apply Helmholtz tomography, which accounts for finite frequency effects, at periods greater than 50 s. Also following Lin *et al.* (2009), the uncertainties in the isotropic maps are scaled up to encompass the differences between the ambient noise and earthquake-derived maps.

An example of the output of eikonal (ambient noise data) and Helmholtz (earthquakes data) tomography for a point in the Basin and Range province (Point A, Fig. 3a) is shown in Fig. 2 in which

the local azimuthal variation of Rayleigh wave phase velocity is presented at three periods, where results at 10 s are from ambient noise, at 50 s from earthquake data, and at 32 s period from a combination of ambient noise and earthquake data. At each period for each location a truncated Fourier series is fit to the data to estimate the azimuthal dependence of phase velocity for both Rayleigh and Love waves:

$$c(T, \psi) = c_0(T)[1 + a_2 \cos(2(\psi - \varphi_{FA})) + a_4 \cos(4(\psi - \alpha))], \quad (3)$$

where T is period, ψ is the azimuth of propagation of the wave measured clockwise from north, c_0 is isotropic phase speed, φ_{FA} is what we call the 2ψ fast axis direction, α is an analogous phase angle for 4ψ variations in phase speed, and a_2 and a_4 are the relative amplitudes of the 2ψ and 4ψ anisotropy. Uncertainties in each of these quantities are determined at each location and period.

Examples of isotropic phase speed maps for Rayleigh and Love waves are presented in Fig. 3, where the short period maps (10 s period) are determined from ambient noise, the long period maps (Rayleigh: 70 s, Love: 45 s) are from earthquake data, and the intermediate period maps are a combination of both data sets. Although azimuthally anisotropic phase speed maps are estimated for both Rayleigh and Love waves, we use only the 2ψ maps for Rayleigh waves here. Rayleigh wave azimuthal anisotropy is observed to be dominated by 180° periodicity (or 2ψ anisotropy) as expected for weakly anisotropic media (Smith & Dahlen 1973). For Love waves, we use only the azimuthally isotropic phase speed maps because Love wave anisotropy is dominated by 90° periodicity (or 4ψ anisotropy), which is a more difficult observable that we choose not to invoke (comparing with Rayleigh wave, the observation of azimuthally dependent Love wave requires better azimuthal data coverage, while the horizontal component of the data is typically noisier than the vertical component). Examples of observations of Rayleigh wave azimuthal anisotropy are presented in Fig. 4 at three periods, where the length of each bar is the peak-to-peak amplitude of 2ψ anisotropy, $2a_2$, and the orientation of each bar is the fast axis direction φ_{FA} .

Examples of characteristic maps (Rayleigh: 32 s period, Love: 25 s period) of the estimated uncertainties in these quantities are presented in Fig. 5. The spatially averaged uncertainties in the isotropic Rayleigh and Love wave speeds (Figs 5a and b) are 8 and 18 m s^{-1} , respectively, illustrating that Love wave uncertainties are

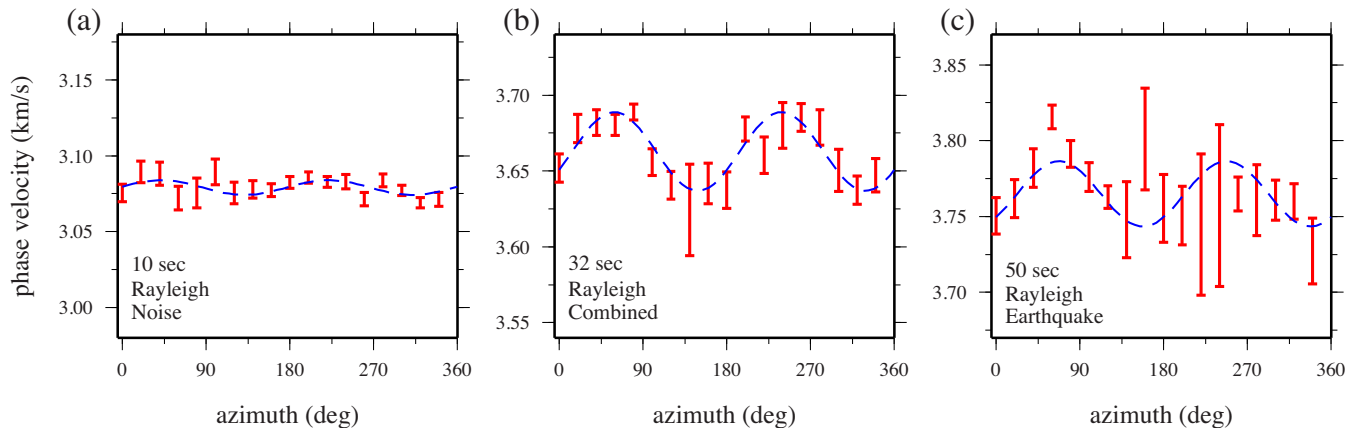


Figure 2. Examples of 10, 32 and 50 s period Rayleigh wave phase velocity observations as a function of azimuth for location A identified in Fig. 3(a), observed using ambient noise data, the combination of ambient noise and earthquake data and earthquake data, respectively. Blue dashed lines give the best-fitting 2ψ curves, where ψ is the azimuth of wave propagation defined positive clockwise from north.

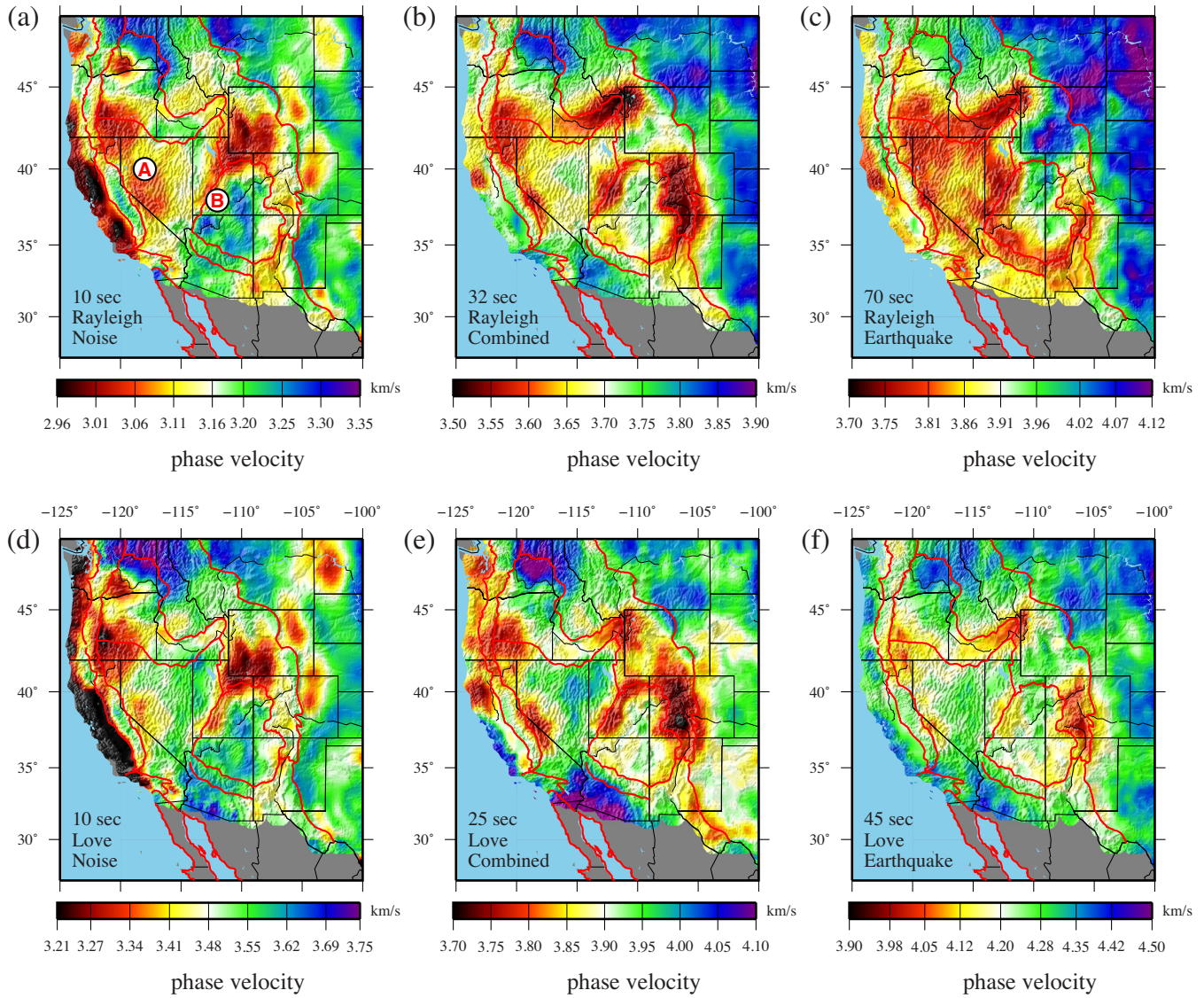


Figure 3. Examples of Rayleigh and Love wave isotropic phase speed maps. (a)–(c) Rayleigh wave phase speed maps at 10, 32 and 70 s period derived from ambient noise data, the combination of ambient noise and earthquake data and earthquake data, respectively. (d)–(f) Love wave phase speed maps at 10, 25 and 45 s period, similarly defined from ambient noise data, the combination of ambient noise and earthquake data and earthquake data, respectively.

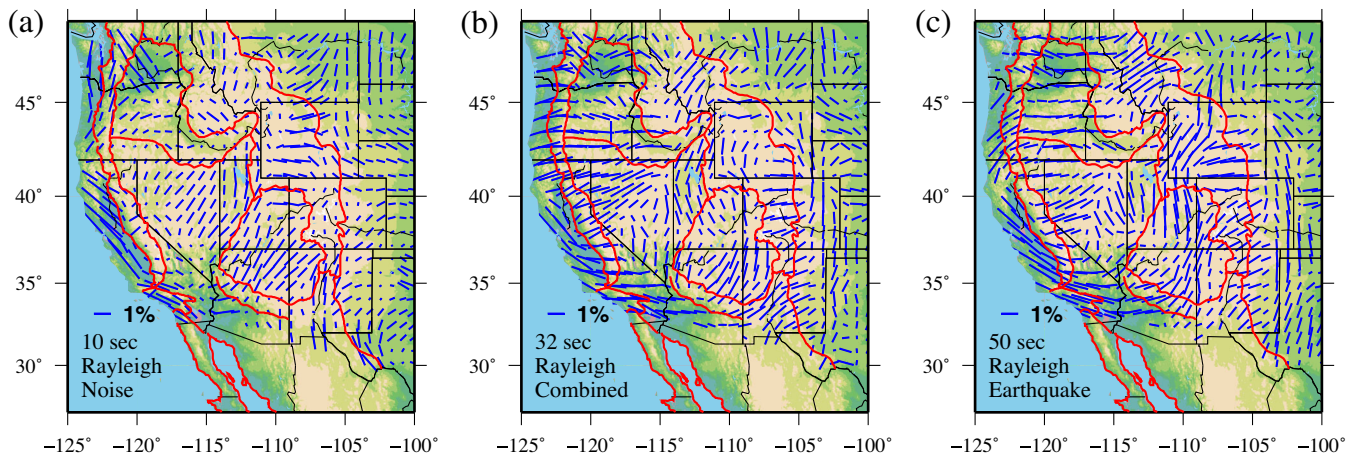


Figure 4. The observed Rayleigh wave 2ψ azimuthal anisotropy maps, where ψ is the azimuth of wave propagation defined positive clockwise from north. (a)–(c) Rayleigh wave azimuthal anisotropy maps at 10, 32 and 50 s period derived from ambient noise data, the combination of ambient noise and earthquake data and earthquake data, respectively. The bars are Rayleigh wave fast directions with lengths representing the peak-to-peak amplitude (in per cent).

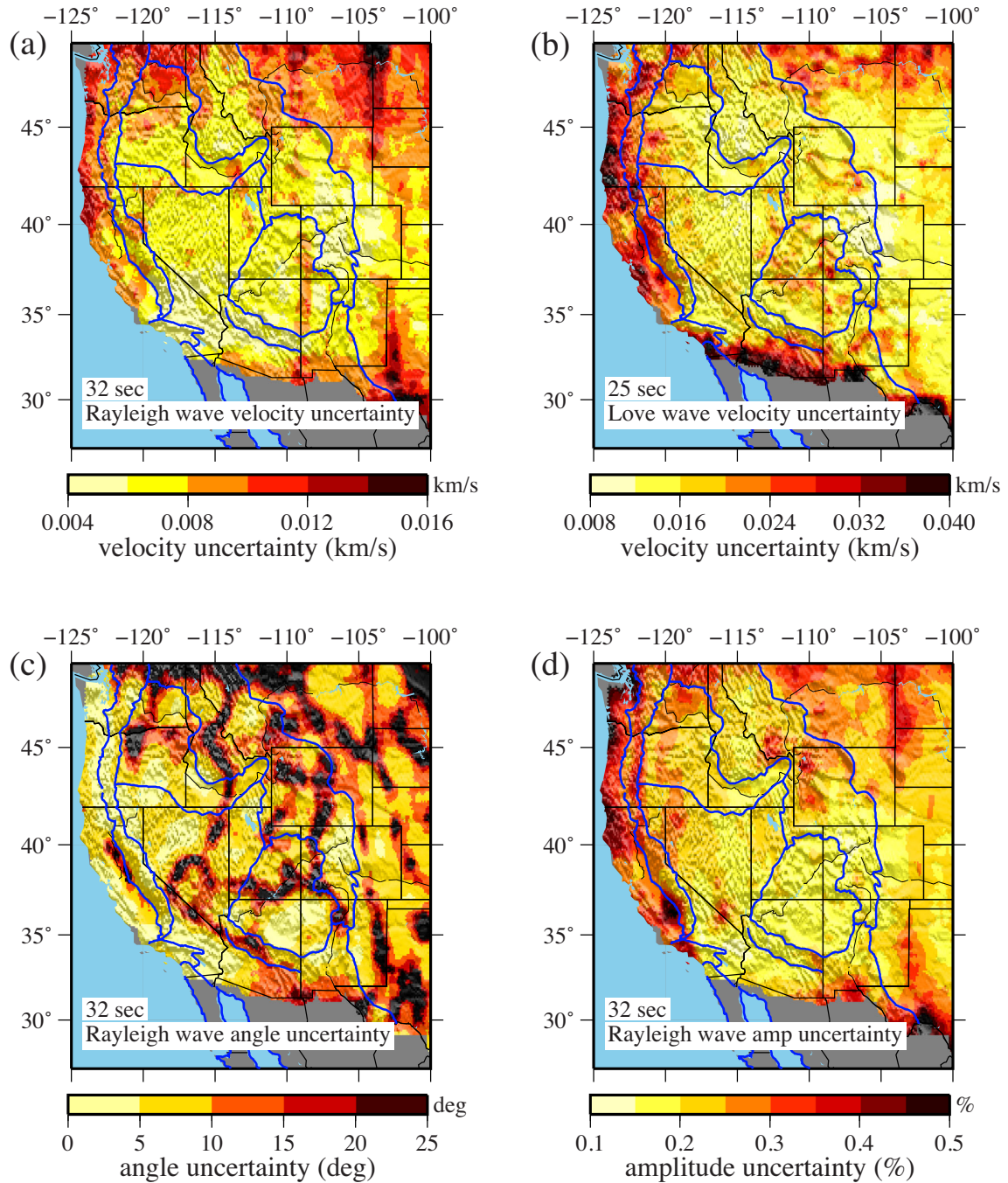


Figure 5. Uncertainty maps for (a) the isotropic Rayleigh wave phase speeds at 32 s period, (b) the isotropic Love wave phase speed at 25 s period, (c) the fast azimuth direction of Rayleigh wave azimuthal anisotropy at 32 s period and (d) the amplitude of Rayleigh wave azimuthal anisotropy at 32 s period.

typically more than twice as large as Rayleigh wave uncertainties. Uncertainties in the fast axis directions depend on the amplitude of azimuthal anisotropy and the regions of large uncertainty in Fig. 5(c) occur where the amplitude of azimuthal anisotropy is small. The average peak-to-peak amplitude of 2ψ anisotropy for the 32 s Rayleigh wave is approximately 0.8 per cent, and for this amplitude the uncertainty of the fast axis direction averages about 8° . The uncertainty grows sharply as the amplitude of anisotropy reduces below about 0.5 per cent and diminishes slowly as the amplitude grows above 1 per cent. The average uncertainty in the amplitude of 2ψ anisotropy for the 32 s Rayleigh wave is about 0.24 per cent, which is less than $1/3$ of the average amplitude of anisotropy. Thus,

the amplitude of the 2ψ Rayleigh wave anisotropy is determined typically to better than 3σ .

From the maps of isotropic phase speed for Rayleigh and Love waves and the amplitude and fast axis direction of 2ψ anisotropy for Rayleigh waves (and their uncertainties), we generate at location on a $0.2^\circ \times 0.2^\circ$ grid in the study area isotropic phase speed curves (dispersion curves) for both Rayleigh and Love waves and 2ψ anisotropic period-dependent curves for Rayleigh waves. This raw material forms the basis for the later inversion for a 3-D model. Fig. 6 presents examples for two locations (A: Basin and Range, B: Colorado Plateau identified in Fig. 3a) that illustrate how these curves can vary. For Point A, the fast azimuth of the Rayleigh

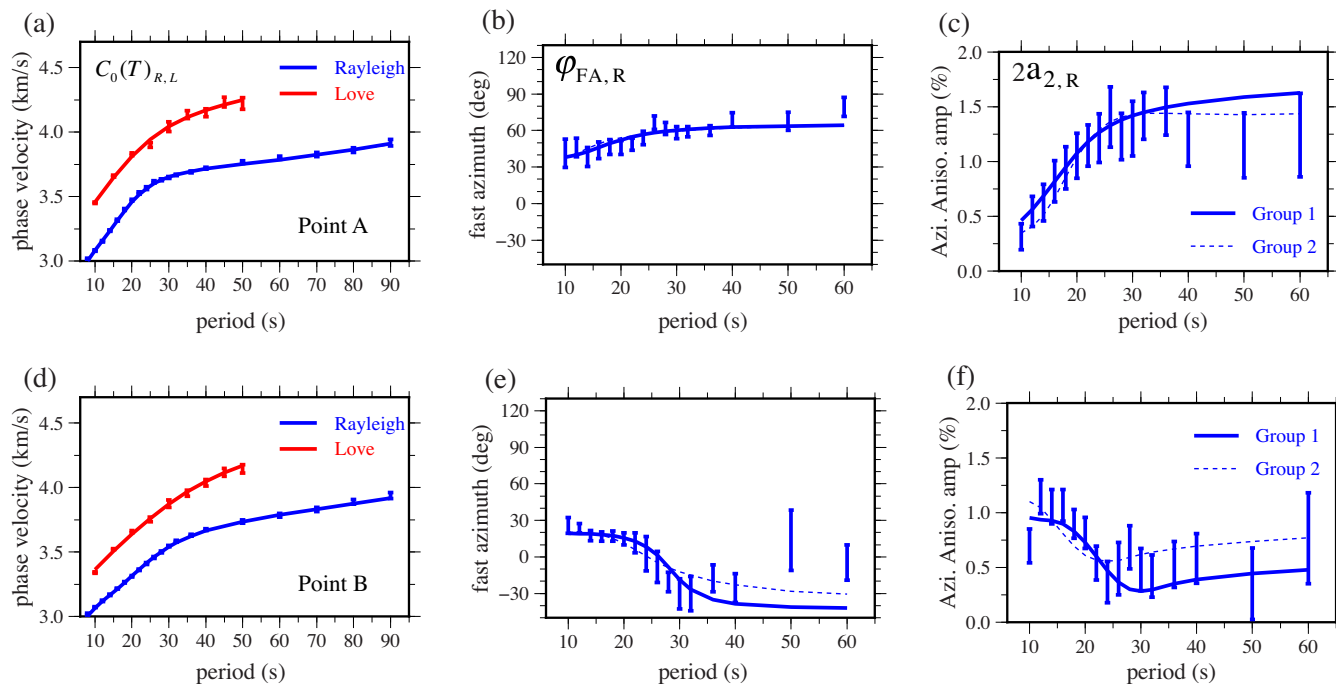


Figure 6. (a–c) The local dispersion curves for Point A in the Basin and Range province (identified in Fig. 3a). The local (a) phase speed, (b) fast azimuth direction and (c) azimuthal anisotropy amplitude curves are presented as one-standard deviation error bars. Red error bars are the Love wave data and blue error bars are the Rayleigh wave data. The solid and dashed lines are the dispersion curves computed from the average of the posterior distribution for Point A: solid lines are from Group 1 models while dashed lines are from Group 2 models (defined in Section 4). (d–f) Similar to (a–c) but for Point B in the Colorado Plateau (Fig. 3a).

wave does not change strongly with period, but the amplitude of azimuthal anisotropy increases with period. In contrast, for Point B, the fast azimuth changes with period, but the amplitude of azimuthal anisotropy tends to decrease with period.

Similar data sets have been used previously to study the anisotropic structure of the western United States. For example, Moschetti *et al.* (2010a,b) used isotropic Rayleigh and Love wave phase speed dispersion curves such as those presented in Figs 6(a) and (d) to image apparent crustal radial anisotropy. Lin *et al.* (2011) used azimuthally anisotropic dispersion curves similar to those in Figs 6(b), (c), (e) and (f) to image the apparent crustal and uppermost mantle azimuthal anisotropy. These two data sets were interpreted separately, but here we attempt to explain both radial and azimuthal anisotropy simultaneously using tilted hexagonally symmetric media (Fig. 1).

3 THE ELASTIC TENSOR AND SURFACE WAVE ANISOTROPY

In a linearly elastic medium, stress and strain are related by a linear constitutive equation, $\sigma_{ij} = C_{ijkl}\epsilon_{kl}$, where C_{ijkl} is the elastic tensor that describes the behaviour of the medium under strain and, therefore, determines the speed of seismic waves. Without loss of generality, the elastic tensor can be compacted into the 6×6 elastic modulus matrix, $C_{\alpha\beta}$, following the Voigt recipe (e.g. Thomsen 1986). Although a general elastic tensor is described by 21 elastic moduli, hexagonal symmetry is often used to characterize Earth materials due to its simplicity (e.g. Dziewoński & Anderson 1981; Montagner & Nataf 1988), and can approximate many media within the Earth (e.g. laminated structures, LPO of mica or micaceous rocks, alignment of olivine crystals along the a axis with randomly oriented b and c axes). The hexagonally symmetric elastic modulus matrices with vertical ($^V C_{\alpha\beta}$) and horizontal ($^H C_{\alpha\beta}$) symmetry axes

are presented in Section 1. A general reorientation of the symmetry axis, which we call a tilt, is achieved by rotating $^V C_{\alpha\beta}$ through the dip and strike angles defined in Fig. 1(a), as described in the Appendix. The elastic constants for a tilted hexagonally symmetric medium can be characterized by seven independent parameters, five unique elastic constants (A , C , N , L , F) that describe the un-tilted hexagonally symmetric (transversely isotropic) elastic tensor, and two for the orientation of the symmetry axis (Montagner & Nataf 1988).

For a model of the elastic tensor as a function of depth at a given location, the forward problem in which period and azimuth dependent Rayleigh and Love wave phase speed curves are computed is described in the Appendix. For weakly anisotropic media, surface wave velocities are only sensitive to 13 elements of the elastic tensor and the remaining 8 elements are in the null space of surface wave velocities (Montagner & Nataf 1986). There is an additional symmetry in surface wave observations: phase speeds with dip angles of θ and $\pi - \theta$ (with constant ϕ) are indistinguishable, as are observations at strike angles of ϕ and $\pi + \phi$ (with constant θ). This means that surface wave observations cannot distinguish between the left-dipping foliation plane in Fig. 1(a) from a right-dipping foliation plane that has been rotated about the z -axis by 180° .

Some terminology is needed to help distinguish between the properties of the anisotropic medium from observations of anisotropy with surface waves. By ‘inherent anisotropy’ we mean the anisotropy of the untilted hexagonally symmetric elastic tensor given by the moduli A , C , N , L , F . We often summarize the inherent anisotropy of a hexagonally symmetric medium using the Thomsen parameters (Thomsen 1986; Helbig & Thomsen 2005; Thomsen & Anderson 2015):

$$\varepsilon \equiv \frac{A - C}{2C} \approx \frac{V_{PH} - V_{PV}}{V_P} \quad (4)$$

$$\gamma \equiv \frac{N - L}{2L} \approx \frac{V_{SH} - V_{SV}}{V_S} \quad (5)$$

$$\delta \equiv \frac{(F + L)^2 - (C - L)^2}{2C(C - L)} \approx \frac{F + 2L - C}{C}, \quad (6)$$

where ε is referred to as inherent ‘ P -wave anisotropy’ and γ is called inherent ‘ S -wave anisotropy’. A so-called ‘elliptical’ anisotropic medium is one in which $\delta = \varepsilon$, in which case P wave and SH wave fronts are elliptical and SV wave fronts are spherical (Thomsen 1986). As shown in the Appendix, upon tilting and reorienting in strike angle, a hexagonally symmetric elastic tensor can be decomposed into the sum of an azimuthally invariant (or effective transversely isotropic) tensor and an azimuthally anisotropic tensor. We refer to the moduli that compose the azimuthally invariant tensor ($\hat{A}, \hat{C}, \hat{N}, \hat{L}, \hat{F}$) as the ‘apparent’ transversely isotropic moduli because these moduli govern the azimuthally averaged phase speeds of Rayleigh and Love waves. The Thomsen parameters can be recomputed using these moduli and they define apparent quasi- P - and quasi- S -wave radial anisotropy: $\hat{\varepsilon} \equiv (\hat{A} - \hat{C})/2\hat{C}$, $\hat{\gamma} \equiv (\hat{N} - \hat{L})/2\hat{L}$. As discussed later, previous observational studies of radial anisotropy have estimated apparent radial anisotropy rather than the inherent anisotropy of the medium if Earth media are, in fact, not oriented with a vertical symmetry axis.

A tilted hexagonally symmetric elastic tensor will generate both radial and azimuthal anisotropy in surface waves. Fig. 1(b) demonstrates how apparent SV-wave azimuthal and apparent S -wave radial anisotropy (Rayleigh-Love discrepancy) vary as a function of dip angle. Note that only the dip angle is changing so that the inherent anisotropy is constant as apparent anisotropy changes. These curves are computed from a simple elastic tensor with a slow symmetry axis. For this model, the amplitude of azimuthal anisotropy increases with increasing dip angle (θ), and the apparent radial anisotropy decreases with increasing dip angle. When the dip angle is 0, there is strong positive apparent S -wave radial anisotropy but no azimuthal anisotropy. At some dip angle, the apparent radial anisotropy vanishes but the azimuthal anisotropy is non-zero. As the dip angle increases further, the apparent radial anisotropy becomes negative (meaning $\hat{L} > \hat{N}$) and azimuthal anisotropy attains its maximum value. This example is intended to qualitatively illustrate the trend with dip angle; the details (e.g. the absolute amplitude, the crossing point in dip angle, and the number of crossing points) depend on the elastic tensor itself (especially F or η).

The computation of Rayleigh and Love wave phase velocities from a given tilted hexagonally symmetric medium is discussed in the Appendix.

4 MODEL PARAMETRIZATION AND CONSTRAINTS IN THE INVERSION

Our model parametrization, as well as the allowed variations in the model, are similar to those described by Shen *et al.* (2013a,b) in the inversion of isotropic Rayleigh wave phase speeds and receiver functions for an isotropic apparent V_{SV} model of the crust and uppermost mantle in the western and central United States. In fact, our model covers a subset of the region of Shen’s model, which is the starting model for the inversion performed in this paper. Shen’s model is isotropic with $V_S^0 = V_{SH} = V_{SV}$, $\eta^0 = 1$ and $V_P^0 = V_{PV} = V_{PH} = 2.0V_S$ in the sediments, $V_P^0 = V_{PV} = V_{PH} = 1.75V_S$ in the crystalline crust and mantle, density is computed through depth-dependent empirical relationships relative to V_S (Christensen & Mooney 1995; Brocher 2005), and the Q model is taken from the

AK135 model (Kennett *et al.* 1995). Here, we fix the density and Q models to those values found by Shen.

In the crust and mantle we assume that the elastic tensor possesses hexagonal symmetry with orientation given by the dip and strike angles (Fig. 1a). The depth dependence of the elastic moduli A , C , N , L and F (or V_{PV} , V_{PH} , V_{SH} , V_{SV} and η) is represented by four B-splines in the crystalline crust from the base of the sediments to Moho, and five B-splines in the mantle from Moho to 200 km depth. Beneath 200 km the model is identical to AK135. The B-spline basis set imposes a vertical smoothing constraint on the model in both the crust and the mantle. If sedimentary thickness in Shen’s model is less than 5 km, then the sediments are isotropic and are fixed to the 3-D starting model (Shen *et al.* 2013b) in which the depth dependence of V_S is represented by a linear function. Otherwise, as described below, S -wave anisotropy is introduced in the sediments by varying V_{SH} .

In addition to the parametrization, there are model constraints that govern the allowed variations around the starting model (V_S^0 , V_P^0 , η^0) in the inversion (described in the next section). Because we perform a Monte Carlo inversion, which involves only forward modelling, the imposition of the constraints is straightforward as they affect only the choice of models that we compare with data; that is, which models are used to compute the likelihood function. In the following, when referring to the seismic velocities ($V_{PV} = \sqrt{C/\rho}$, $V_{PH} = \sqrt{A/\rho}$, $V_{SV} = \sqrt{L/\rho}$, $V_{SH} = \sqrt{N/\rho}$) and $\eta = F/(A-2L)$ we mean the inherent elements of a hexagonally symmetric elastic tensor; that is, the inherent characteristics of the elastic tensor prior to tilting.

The constraints that are imposed during inversion are the following: (1) Constancy of tilt angles in the crust and mantle: At each location, the dip and strike angles (tilt angles θ , ϕ) that define the orientation of the symmetry axis of anisotropy are constant through the crystalline crust and constant through the mantle, although the crustal and mantle angles are allowed to differ from each other. (2) Range of model variables: The allowed variations of the elastic parameters in the crystalline crust and mantle relative to the starting model are as follows: $V_{SV} \pm 0.05V_S^0$, $V_{SH} \pm 0.15V_S^0$, $V_{PV} \pm 0.15V_P^0$ and $V_{PH} \pm 0.15V_P^0$. In addition, in the crust $\eta_{\text{crust}} \in [0.6, 1.1]$ and in the mantle it lies in the smaller range $\eta_{\text{mantle}} \in [0.85, 1.1]$. Also, the tilt angles range through the following intervals: $\theta \in [0^\circ, 90^\circ]$, $\phi \in [0^\circ, 180^\circ]$. The reasons for the choice of the ranges of model variables are explained in subsequent paragraphs. (3) Sedimentary model: If sedimentary thickness is less than 5 km in Shen’s model, the sedimentary part of the model remains unchanged (i.e. it is isotropic and identical to Shen’s model). If the thickness is greater than 5 km, then only the V_{SH} part of the model is perturbed to introduce S -wave radial anisotropy with $\gamma \in [0, 0.2]$; that is, this is a maximum S -wave anisotropy of 20 per cent. No tilt is introduced to the elastic tensor in the sediments. (4) V_P/V_S ratio: $V_P/V_S \approx (V_{PV} + V_{PH})/(V_{SV} + V_{SH}) \in [1.65, 1.85]$. (5) Monotonicity constraint: V_{SV} , V_{SH} , V_{PV} and V_{PH} each increase monotonically with depth in the crystalline crust. A monotonicity constraint is not imposed on η or on any of the variables in the mantle. (6) Positive inherent anisotropy: $V_{SH} > V_{SV}$, $V_{PH} > V_{PV}$. This indicates that our inverted hexagonally symmetric tensor has a slow symmetry axis ($N > L$, $A > C$, V_P and V_S are slower in the direction of symmetry axis and faster in the foliation plane). (7) Fixed points of the model: Density, sedimentary thickness and crustal thickness are not changed relative to the starting model.

The constraints can be considered to fall into two groups, one group is based on prior knowledge and the other is introduced to simplify the model. The V_P/V_S ratio, positive anisotropy, and the

fixed points of the model constraints are based on prior knowledge. For example, the inherent anisotropies are set to be positive (slow symmetry axis) because most crustal rock samples display slow velocities perpendicular to the foliation plane and fast velocities within the foliation plane, and anisotropy caused by layering requires positive inherent anisotropy (Tatham *et al.* 2008; Brownlee *et al.* 2011; Erdman *et al.* 2013; Thomsen & Anderson 2015). In addition, we have tested negative inherent anisotropy (fast symmetry axis), which is probably consistent with crustal rocks abundant in quartz and amphibole, but this kind of medium cannot explain our observations across the region of study. We set the sedimentary thickness and crystalline crustal thickness constant based on the receiver function observations by Shen *et al.* (2013b). The V_P/V_S ratio is constrained to be within 1.65–1.85 because most observations of V_P/V_S fall in this range (e.g. Christensen 1996; Lowry & Pérez-Gussinyé 2011; Buehler & Shearer 2014).

In contrast, constraints such as the vertically constant tilt angle in the crust and mantle and the monotonic increase of seismic wave speeds in the crust are used to simplify the resulting models. Everything else being equal, we prefer simpler models because they are more testable and falsifiable. For example, we could have parametrized the tilt angles as depth-varying and still fit our data. (In fact, there are always an infinite number of possible and more complex alternatives that include more ad hoc assumptions.) Without prior knowledge, more complex models can hardly be proven wrong because they can always fit the data. Besides, little can be learned from such complexities because they are not derived from the data. On the other hand, a simple model cannot always fit the data (e.g. a constant velocity profile cannot fit the dispersion curves), so it is easier to prove wrong (if it is). When a model is too simple to fit the data, we then add complexity to the model or loosen constraints. Because this kind of added complexity is motivated by the data, it is more likely to provide information about the Earth. Therefore, we view the vertically constant tilt angle and monotonicity constraints as hypotheses that we test empirically. If we are unable to fit aspects of the data acceptably, we will return and loosen these constraints to help fit the data. Otherwise, these constraints are kept to generate a simple model.

In summary, we seek an anisotropic model that is relatively close to the isotropic model of Shen, possesses hexagonally symmetric anisotropy with a slow symmetry axis of locally constant but geographically variable orientation in the crystalline crust and upper mantle, has only positive P -wave and S -wave anisotropy, a V_P/V_S ratio that varies around that of a Poisson solid and possesses seismic velocities that increase with depth in the crust. Given the allowed variations in the elastic moduli, the maximum S -wave anisotropy (γ) considered in both the crust and mantle is 20 per cent. Because Shen's model was constructed with Rayleigh wave data alone (and receiver functions) it only weakly constrains V_P and V_{SH} , but has rather strong constraints on the sedimentary and crustal thicknesses and V_{SV} in the crust. For this reason, we allow in our inversion wider variation in V_{PV} and V_{SH} than in V_{SV} . η is allowed to vary through a wider range in the crust than in the mantle based on measurements of elastic tensors for crustal rocks (Tatham *et al.* 2008; Brownlee *et al.* 2011; Erdman *et al.* 2013) and olivine (Babuška 1991), which is believed to be the major contributor to mantle anisotropy, and also to be consistent with mantle elastic moduli in other studies (e.g. Montagner & Anderson 1989). We do not allow sedimentary thickness or crustal thickness to vary at all because receiver functions are not used in our inversion. However, we find that in areas where the sediments are thicker than 5 km, radial anisotropy is needed in order to fit the data at short periods. In this case, we introduce

only S -wave anisotropy in the sediments (no P -wave anisotropy, no deviation of η from unity), which is probably physically unrealistic, so we do not interpret the resulting model of anisotropy in the sediments. However, regions where sediments are thicker than 5 km in Shen's model are relatively rare in the western United States, being confined to a few regions, most notably southwestern Wyoming.

5 BAYESIAN MONTE CARLO INVERSION

The data that are inverted are similar to those shown in Fig. 6 for two locations in the western United States. We apply a Bayesian Monte Carlo method to invert the data at every location on a $1^\circ \times 1^\circ$ grid. The implementation of the inversion is very similar to the method described in detail by Shen *et al.* (2013a), but we do not apply receiver functions. We construct observations such as those in Fig. 6 on a $0.2^\circ \times 0.2^\circ$ grid. The isotropic model constructed by Shen *et al.* (2013b), which is our starting model, is constructed on the irregular grid given by the station locations where the receiver functions are defined. In contrast, we construct our model on a regular $1^\circ \times 1^\circ$ grid across the central and western United States. At each grid point, the starting model in our inversion is Shen's model at the nearest station, which in some cases may be as much as 40 km away.

At each location the prior probability distribution is defined relative to Shen's model based on the constraints described in the previous section. The prior distribution guides the sampling of model space. A model is determined to be acceptable or not based on its likelihood function $L(m)$, which is related to the chi-squared misfit $S(m)$ (Shen *et al.* 2013a; Xie *et al.* 2013). $L(m)$ and $S(m)$ are defined as follows:

$$L(m) = \exp \left[-\frac{1}{2} S(m) \right], \quad (7)$$

where

$$S(m) = \sum_i \frac{[D(m)_i^{\text{predicted}} - D_i^{\text{observed}}]^2}{\sigma_i^2}. \quad (8)$$

The chi-squared misfit $S(m)$ measures the weighted difference between the observed and predicted dispersion curves, where the forward model is computed as described in the Appendix. The chi-squared misfit is composed of four terms, corresponding to the four curves at each location shown in Fig. 6. The first two are for isotropic Rayleigh and Love waves. The other two are for the amplitude and fast-axis direction of Rayleigh wave azimuthal anisotropy. The only weights in the misfit function are the standard deviations of the measurements.

The model sampling process and acceptance criteria follow the procedure described by Xie *et al.* (2013) where the partial derivatives are updated when each additional 200 models are accepted. Because the model sampling will not complete until at least 5000 models are initially accepted, the partial derivatives are updated at least 25 times during the sampling. After the sampling is complete, the entire set of initially accepted models is put through the selection process again to remove models with larger misfit (Xie *et al.* 2013). On average, models are accepted up to about twice the rms misfit of the best-fitting model. This reselected model set composes the (truncated) posterior probability distribution, which is the principal output of the inversion. The posterior distribution satisfies the constraints and observations within tolerances that depend on data uncertainties.

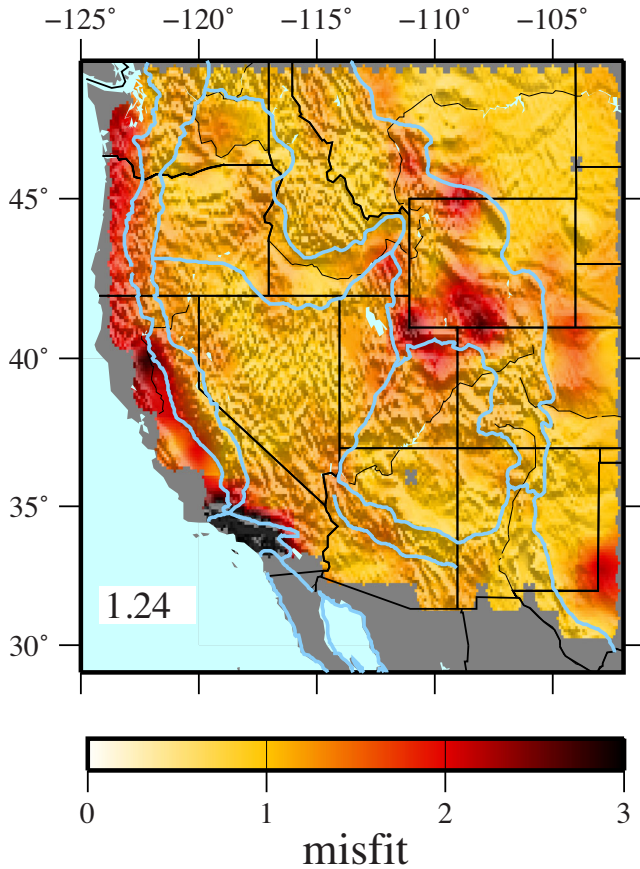


Figure 7. Map view of the misfit for the best-fitting models (from Group 1 models) across the study region. The misfit is defined as $\sqrt{S/N}$ where S is the chi-squared misfit defined in eq. (8), and N is the number of observations. Average value across the map is inset.

Fig. 7 presents map views of the misfit for the best-fitting models (from Group 1, defined below) across the study region. Here the misfit is defined as $\sqrt{S/N}$ where S is the chi-squared misfit defined in eq. (8), and N is the number of observations. In general, our data can be well fit with an average misfit around 1.2. The misfit is larger along the coast and near the Green River Basin and other basins in southwestern Wyoming, where thick sediments exist. This indicates that our parametrization is not optimal in regions with thick sediments. In the future, we plan to improve the inversion in the sediments by incorporating the Rayleigh wave H/V ratio from ambient noise (Lin *et al.* 2012, 2014) that provide additional sensitivity to shallow structures. Misfit from Group 2 (defined below) models is similar.

Examples of prior and posterior probability distributions for the inherent moduli at 20 km depth are shown in Figs 8 and 9 for the same two locations for which we present the data in Fig. 6. The prior distributions are strongly shaped by the model constraints and are displayed as white histograms in each panel. For example, V_{SV} displays a narrower prior distribution because only 5 per cent perturbations relative to the starting model are sampled compared to 15 per cent perturbations in V_{SH} , V_{PV} and V_{PH} . The non-uniform shape of many of the distributions arises from constraints that tie model variables between different depths or of different types, such as the monotonicity constraint. The prior distributions for the dip and strike angles are uniform, however, because they are constant across the crust and, therefore, are not explicitly tied to choices of variables at different depths or of different types. The posterior

distribution is wider for variables that are poorly constrained by the data (e.g. V_{PH} , η) than for those that are well constrained (e.g. θ , ϕ , V_{SV} , V_{SH}). Note that the crustal dip and strike angles, θ and ϕ , are well constrained by the data in that their posterior distributions are relatively narrow. However, the posterior distribution of the crustal strike angle is bimodal, defining two model groups in which strike angles differ by 90° , on average. These two groups of models are presented as blue and red histograms in Figs 8 and 9. The physical cause of this bifurcation is discussed in Section 6.2.

We define ‘Group 1’ (red histograms) to be the set of models with a crustal strike angle that approximately parallels the Rayleigh wave fast direction averaged between 10 and 22 s period. ‘Group 2’ is the set of models with a strike angle that is approximately orthogonal to the Rayleigh wave fast axis direction in this period range. There are subtle differences between the crustal moduli A , C , N and L between the two groups, but much stronger differences in η , dip angle θ and the non-ellipticity parameter ($\varepsilon - \delta$). Typically, Group 1 has larger values of η and more nearly elliptical anisotropy ($\varepsilon \approx \delta$) in the crust, whereas Group 2 has smaller η and a more non-elliptical anisotropy. Also, Group 1 models tend to have a slightly larger crustal dip angle, on average. We believe that the bifurcation in model space is controlled fundamentally by η , which is poorly constrained in the prior distribution or by the data. The effect of the bifurcation on our conclusions also will be discussed further in the next section of the paper.

Ultimately, we summarize each posterior distribution by its mean and standard deviation, which define the final model and uncertainty at each depth, and for each model variable. Table 1 presents these statistics for the posterior distributions shown in Figs 8 and 9. Fig. 10 presents vertical profiles of inherent V_{SV} and V_{SH} (related to the moduli L and N), showing the mean and standard deviation for Group 1 and Group 2 models separately at locations A and B in the Basin and Range and Colorado Plateau (Fig. 3a), respectively. Differences between the moduli of the two groups are discussed further below. These profiles are derived to fit the data presented in Fig. 6, where we also show how well the data are fit by the mean model from each group (Group 1: solid lines, Group 2: dashed lines). The two groups fit the isotropic phase speed data nearly identically but do display small differences in the details of the fit to Rayleigh wave azimuthal anisotropy, although both fit within data uncertainties. The differences in fit are largest for the amplitude of azimuthal anisotropy above 30 s period where uncertainties in this variable grow. Note that both groups fit the fast azimuth direction of Rayleigh wave azimuthal anisotropy equally well, even though the strikes angles of the crustal anisotropy differ by 90° .

In addition, posterior covariances between model variables at a particular depth or different depths are also determined from the posterior distributions. In practice, we compute posterior correlation matrices in which the elements of the covariance matrix are normalized by the appropriate standard deviation, which normalizes the diagonal elements of the matrix to unity. We use the terms correlation and covariance interchangeably, however.

As an example, the posterior covariance matrix for five variables (γ , ε , δ , θ , ϕ) at 20 km depth is presented in Fig. 11(a) for a point in the Basin and Range province (point A in Fig. 3a). Most correlations are relatively weak, γ is negatively correlated with ε and δ , ε and δ are strongly positively correlated with each other in order to keep a relatively constant $\varepsilon - \delta$. Importantly, the dip angle θ has no correlation with other variables except δ . A correlation between these two variables is probably not surprising because δ affects the speed of waves propagating at an angle through the medium (oblique to the symmetry axis) and θ orients the medium.

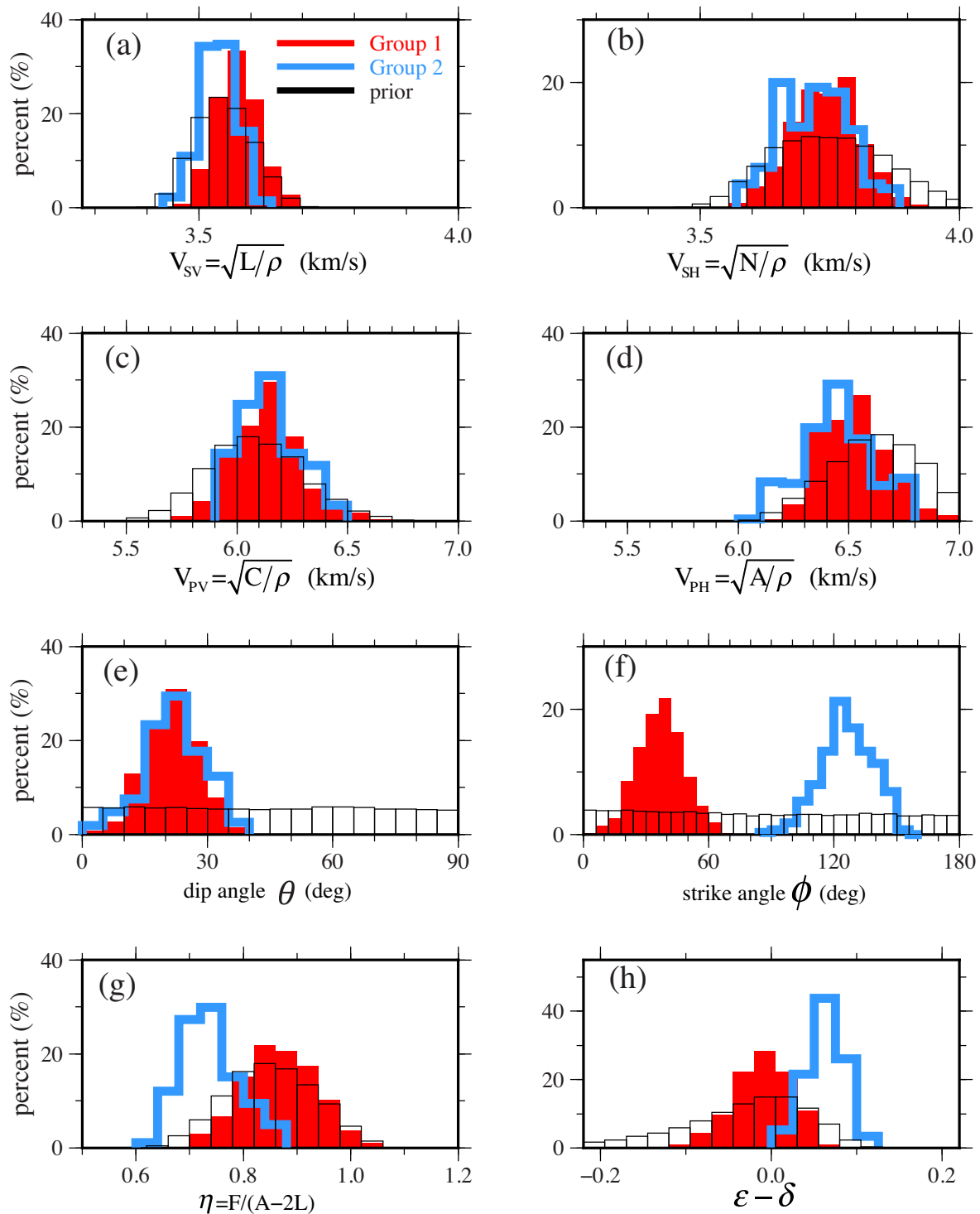


Figure 8. Prior and posterior distributions for several model parameters at 20 km depth for Point A (in the Basin and Range, Fig. 3a). White histograms shown with black lines indicate the prior distributions; both red and blue histograms are the posterior distributions but result from model groups 1 and 2, respectively.

Similarly, Figs 11(b)–(f) shows the posterior covariance matrix for each model variable with itself at different depths. This is again for point A in the Basin and Range province, where crustal thickness is about 31 km; depths greater than 31 km are in the mantle and shallower depths are in the crust. Most of the correlations in this case are positive. The correlation length (a measure of the rate of decay of the covariance with distance) in the crust is smaller than in the mantle because the vertical resolution is better. The B splines in the

crust only span from the bottom of the sediments to the Moho (less than 30 km here), whereas in the mantle they span about 170 km. The correlation length for γ is smaller than for ϵ and δ , indicating a better vertical resolution of γ .

Covariance matrices such as the examples presented here illuminate the implications of the parametrization and constraints imposed in the inversion, but we only interpret this information qualitatively; it is not used formally.

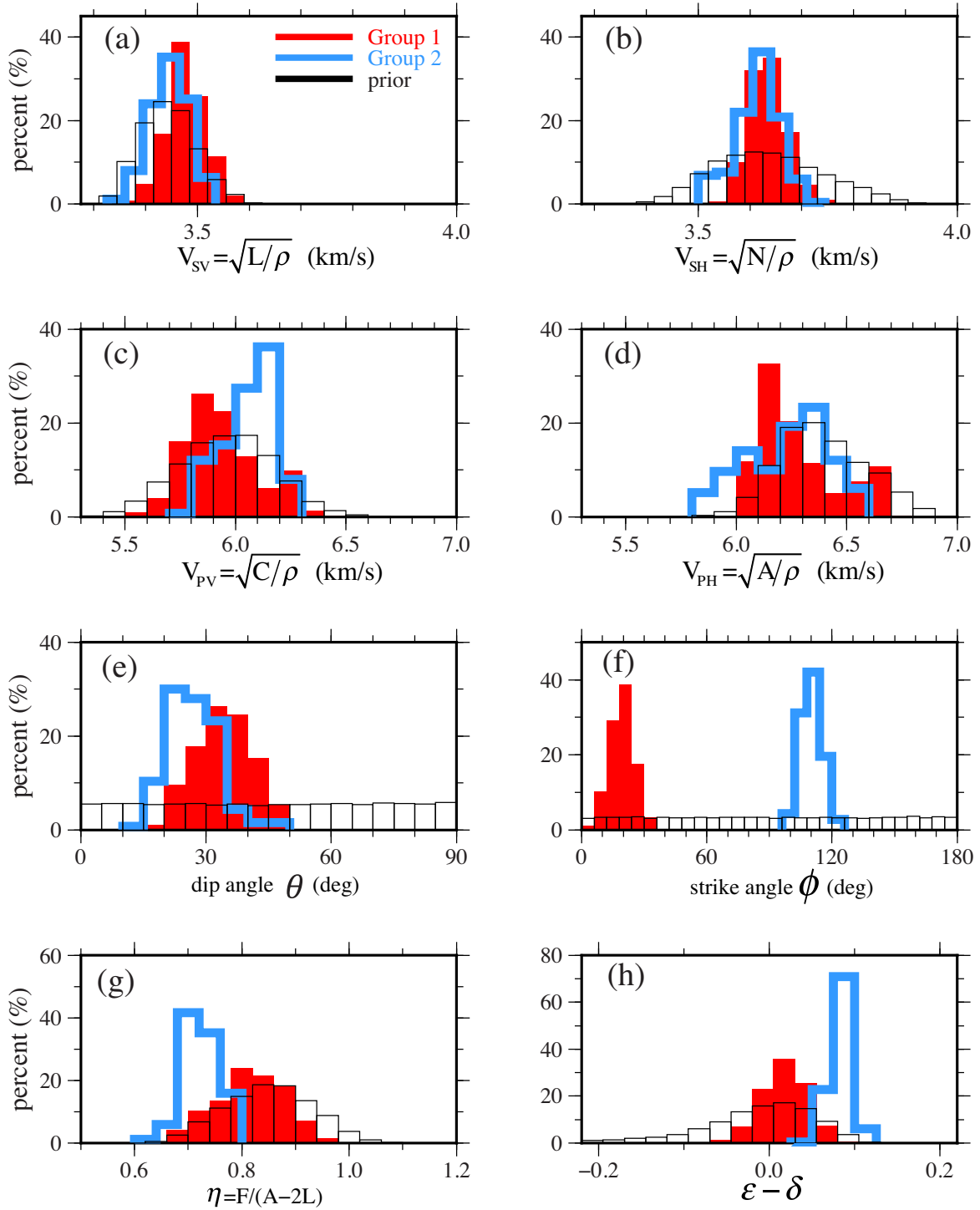
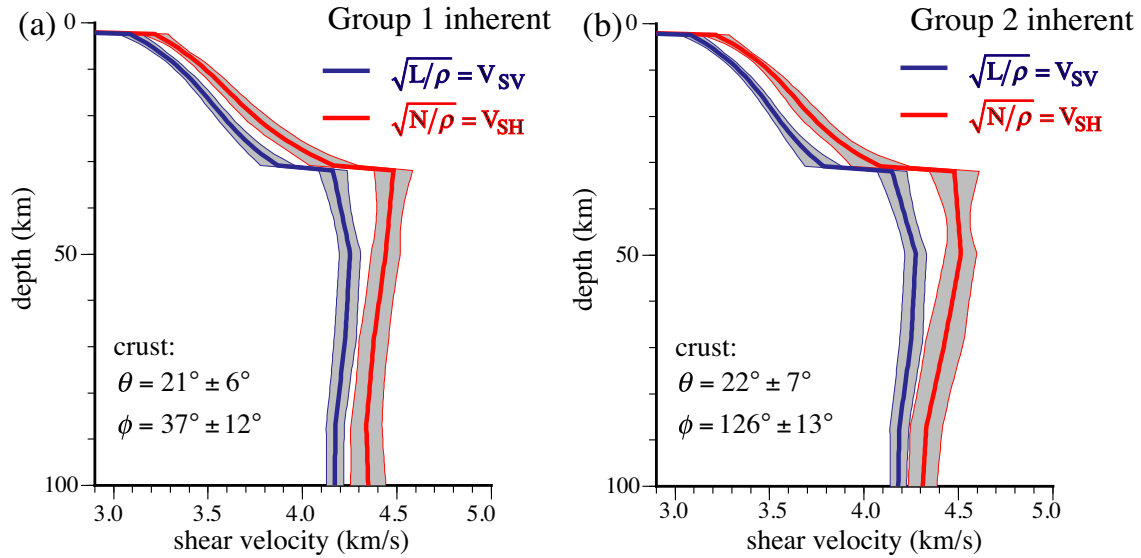


Figure 9. Similar to Fig. 8 but for Point B in the Colorado Plateau (Fig. 3a).

Table 1. The mean and standard deviations for the posterior distributions in Figs 8 and 9.

		$\sqrt{L/\rho} = V_{SV}$ (km s ⁻¹)	$\sqrt{N/\rho} = V_{SH}$ (km s ⁻¹)	$\sqrt{C/\rho} = V_{PV}$ (km s ⁻¹)	$\sqrt{A/\rho} = V_{PH}$ (km s ⁻¹)	Dip angle θ (°)	Strike angle ϕ (°)	$F/(A-2L) = \eta$ Non-ellipticity $\epsilon - \delta$
Point A	$\rho = 2.79 \text{ g cm}^{-3}$							
	Group 1	3.57 (0.04)	3.74 (0.06)	6.14 (0.15)	6.52 (0.15)	21 (6)	37 (12)	0.87 (0.07)
	Group 2	3.54 (0.03)	3.72 (0.07)	6.15 (0.13)	6.47 (0.18)	22 (7)	126 (13)	0.74 (0.05)
Point B	$\rho = 2.73 \text{ g cm}^{-3}$							
	Group 1	3.48 (0.04)	3.63 (0.04)	5.94 (0.17)	6.28 (0.18)	34 (7)	19 (6)	0.82 (0.06)
	Group 2	3.45 (0.04)	3.61 (0.04)	6.06 (0.12)	6.24 (0.19)	27 (6)	110 (5)	0.72 (0.03)

Point A Basin and Range



Point B Colorado Plateau

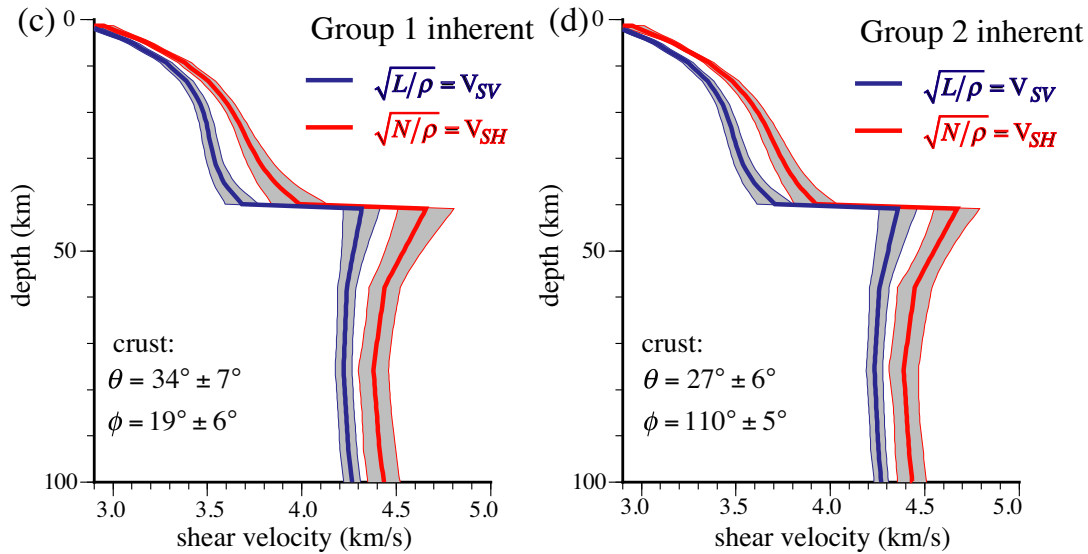


Figure 10. (a) Group 1 posterior distribution at Point A showing the inherent V_{SV} (blue) and V_{SH} (red), where the one-standard deviation extent of the posterior distribution is shown with the grey corridors and the average of each distribution is plotted with bold solid lines. (b) Same as (a), but for Group 2, Point A. (c) Same as (a), but for Group 1, Point B. (d) Same as (a), but for Group 2, Point B. Points A and B are identified in Fig. 3(a).

6 RESULTS

Love wave phase speed dispersion curves extend only up to 50 s period and the Rayleigh wave anisotropic dispersion curves also do not extend to very long periods. Thus, constraints on crustal structure are stronger than on the mantle. We have tested variations in mantle parametrizations and constraints, and found that changes affect estimated crustal structure within uncertainties. In the following, therefore, we will concentrate detailed discussion on the crustal part of our model, and will discuss mantle structure principally in a spatially averaged sense. Later work will specifically aim

to improve and interpret the mantle model in a spatially resolved sense.

6.1 Crustal anisotropy across the western United States

The results presented to this point are only for two locations, in the Basin and Range province and the Colorado Plateau (points A and B, Fig. 3a). We have applied the Bayesian Monte Carlo inversion described above to the United States west of 100°W longitude and produced a 3-D model of the tilted crustal elastic tensor (with

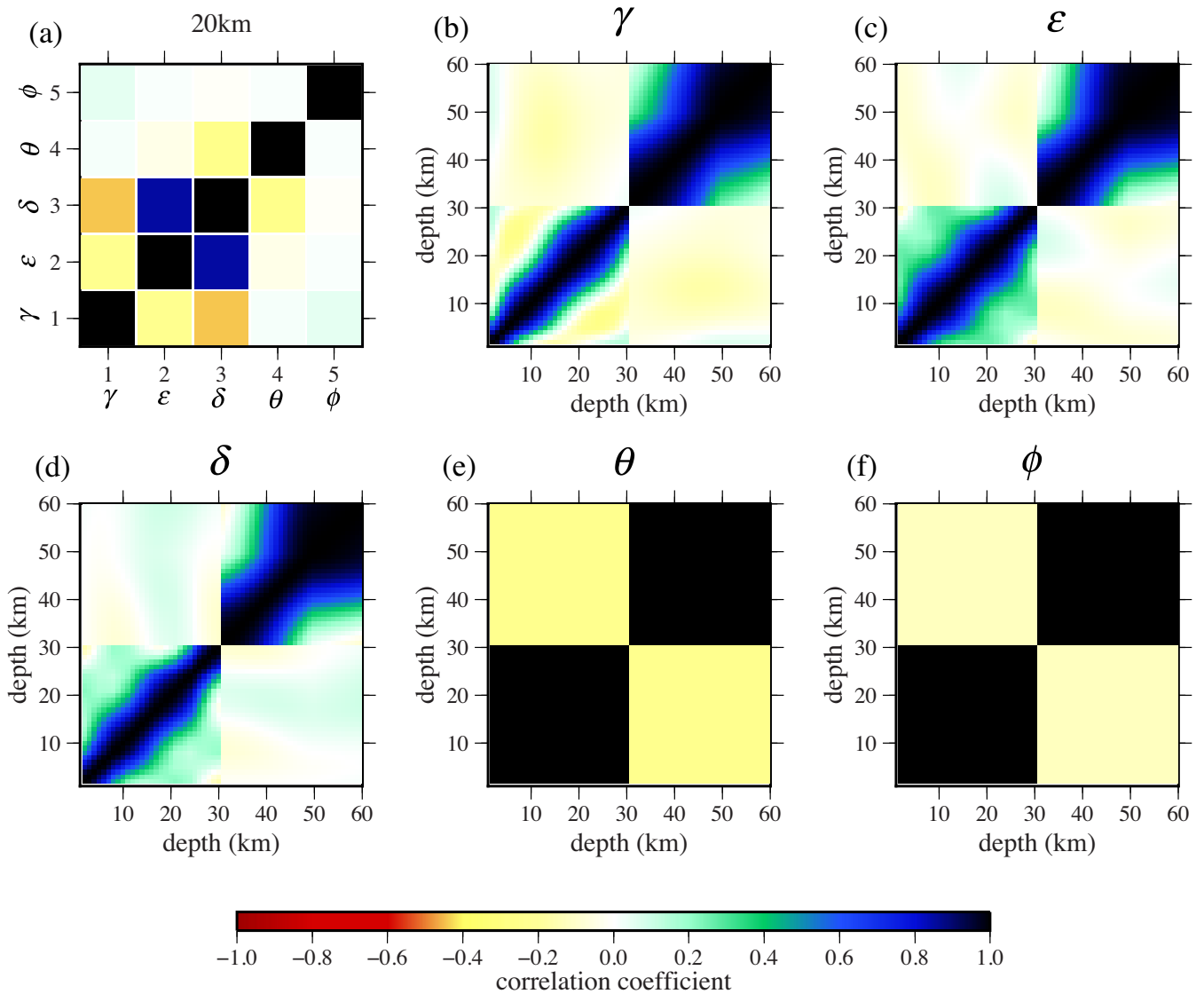


Figure 11. Aspects of the correlation (or normalized covariance) matrix observed at Point A. (a) The correlations between several model parameters at 20 km depth. (b) The correlations between γ at different depths. (c–f) Similar to (b), but for four other model parameters: ε , δ , θ and ϕ . θ is the dip angle, ϕ is the strike angle and γ , ε , δ are Thomsen parameters that summarize the elastic tensor.

uncertainties) on a $1^\circ \times 1^\circ$ grid across the region. The mean and standard deviation of aspects of the posterior distribution averaged across the crystalline crust (from the base of the sediments to Moho) are shown in Figs 12 and 13.

As discussed above, the posterior distribution bifurcates at each location into two disjoint groups of models based on the strike angle, and we present results in the crust for both groups of models. For Group 1, crustal anisotropy is nearly elliptical meaning that the Thomsen parameters ε and δ , defined in eqs (4) and (6), are nearly identical. Fig. 12(a) shows that $\varepsilon - \delta$ is small across the entire western United States for Group 1 models. We refer to $\varepsilon - \delta$ as the ‘non-ellipticity’ parameter because values much larger than zero indicate the deviation from elliptical anisotropy. Group 2 models have more non-elliptical anisotropy as Fig. 12(d) illustrates, and ε is generally greater than δ so that the non-ellipticity parameter is generally positive. The non-ellipticity parameter is about an order of magnitude larger for Group 2 than Group 1 models.

Although the elastic tensors in the two groups of models differ in the extent to which the anisotropy is non-elliptical, the geographical

distribution and the amplitude of inherent S -wave anisotropy, given by the Thomsen parameter γ (eqn. 5), are similar. This amplitude averages about 3.9 per cent for Group 1 and 4.2 per cent for Group 2 (Figs 12b and e). The differences in γ between Groups 1 and 2 are within estimated uncertainties (Figs 13a and d), which average about 2 per cent across the region. On average, γ does not vary strongly with depth in the crust, as Fig. 14 illustrates. The error bars represent the inherent S -wave anisotropy at crustal depths normalized by local crustal thickness averaged across the study region. γ tends to be somewhat stronger in the shallow ($\sim 4 \pm 2$ per cent) and deep ($\sim 6 \pm 3$ per cent) crust than in the middle crust ($\sim 3 \pm 2$ per cent), but the trend is weak and does not occur everywhere. The amplitude of inherent S -wave anisotropy is everywhere positive (as it is constrained to be), and is fairly homogeneous laterally across the western United States. It is, however, largest in the Basin and Range province and smallest in the Colorado Plateau and the western Great Plains. The positivity constraint on γ , motivated by elastic tensors measured on crustal rocks, does not have to be relaxed anywhere to fit the data. γ is larger than its uncertainty across

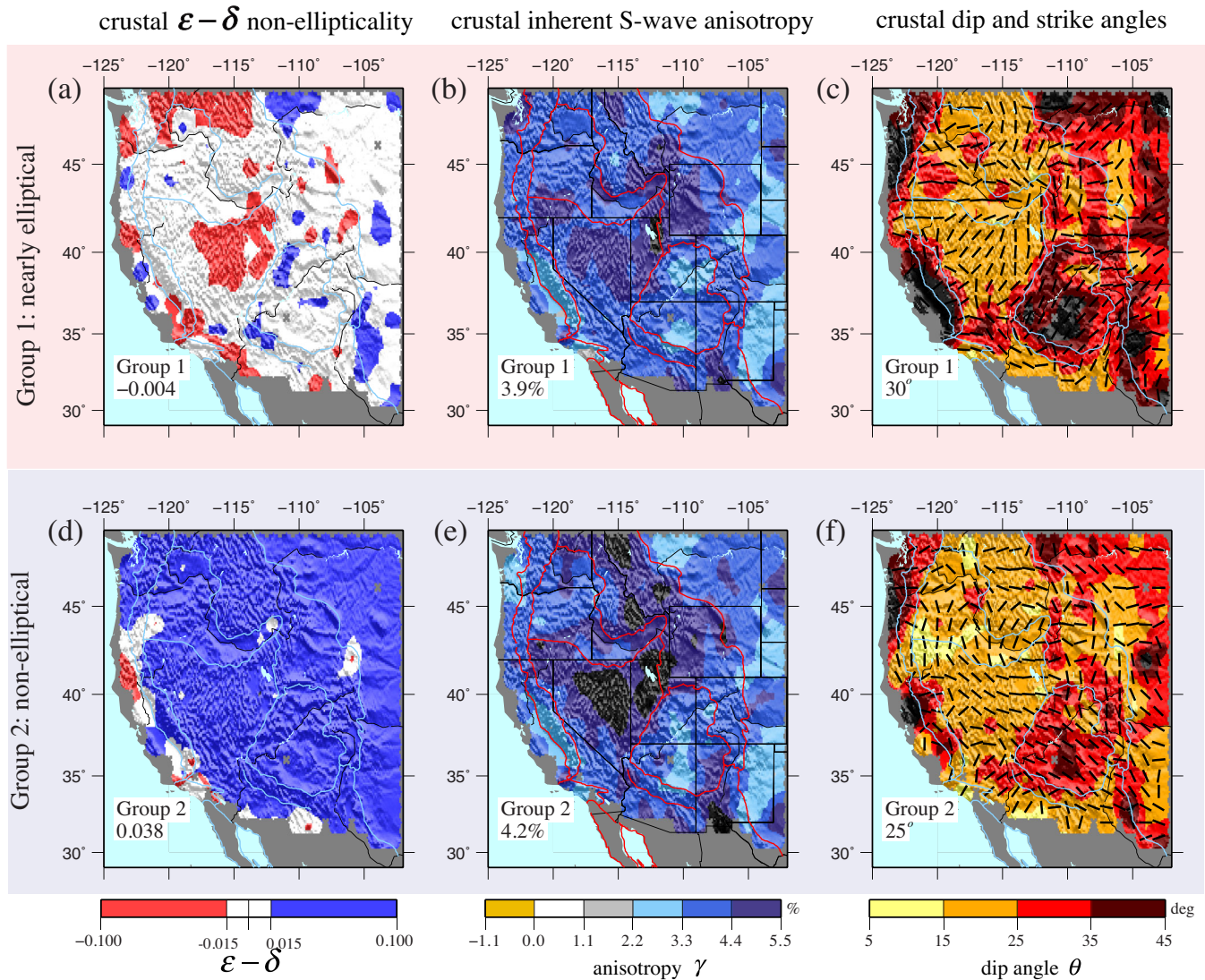


Figure 12. Map view of the crustal averaged non-ellipticity of anisotropy ($\epsilon - \delta$), the crustal averaged inherent S -wave anisotropy (γ), the crustal dip (θ) and strike (ϕ) angles for Group 1 (a–c) and Group 2 (d–f) models. In (c) and (f), dip angles are represented by the background colour and strike angle directions are given by the black bars. Average values across each map are inset.

nearly the entire western United States with the possible exception of some of the peripheral regions where uncertainties grow due to less than ideal data coverage. For this reason, we suggest that γ not be interpreted near the Pacific coast.

Compared with earlier estimates of (apparent) S -wave radial anisotropy across the western United States (e.g. Moschetti *et al.* 2010a,b), the amplitude of γ (inherent S -wave anisotropy) does not change as strongly across the region. This discrepancy is correlated with the difference between ‘inherent’ and ‘apparent’ anisotropy, and is discussed below in Section 6.5.

In contrast with γ , the dip angle θ does change appreciably across the study region and the dip and strike angles differ appreciably between the two model groups. Differences between dip angles, shown by varying the background coloration in Figs 12(c) and (f), are somewhat subtle. The spatially averaged uncertainty in the dip angle across the western United States is 9° – 10° for both model groups. The geographical distribution of the variation in dip angle is similar between the two groups of models, but models in Group 2 have dip angles that average about 25° whereas Group 1 models average about 30° . Recall that the dip angle in

the elastic tensor is introduced to produce azimuthal anisotropy. Thus, elastic tensors with nearly elliptical anisotropy must be tilted more to fit the azimuthal anisotropy data than tensors with substantially non-elliptical anisotropy. The dip angle in the crust everywhere across the western United States is less than about 70° and greater than about 10° , with the majority of the angles falling within the range of 10° and 45° . The Basin and Range province has a shallower dip whereas the Colorado Plateau has a steeper dip, on average.

There is a more prominent difference in strike angle than dip angle between the two groups of models. The strike angle directions for Group 1 and Group 2 models differ by 90° . This is a significant enough observation to warrant its own subsection, and is discussed further in Sections 6.2 and 6.3. Uncertainty in strike angle averages 12° – 13° across the study region.

There are also significant differences between the two groups of models in η and the other Thomsen parameters, ϵ (inherent P -wave anisotropy) and δ . η averages about 0.83 (± 0.08) for Group 1 models and 0.077 (± 0.07) for Group 2. In addition, there are larger values of inherent P -wave anisotropy (ϵ) in Group 1 (8.1 \pm

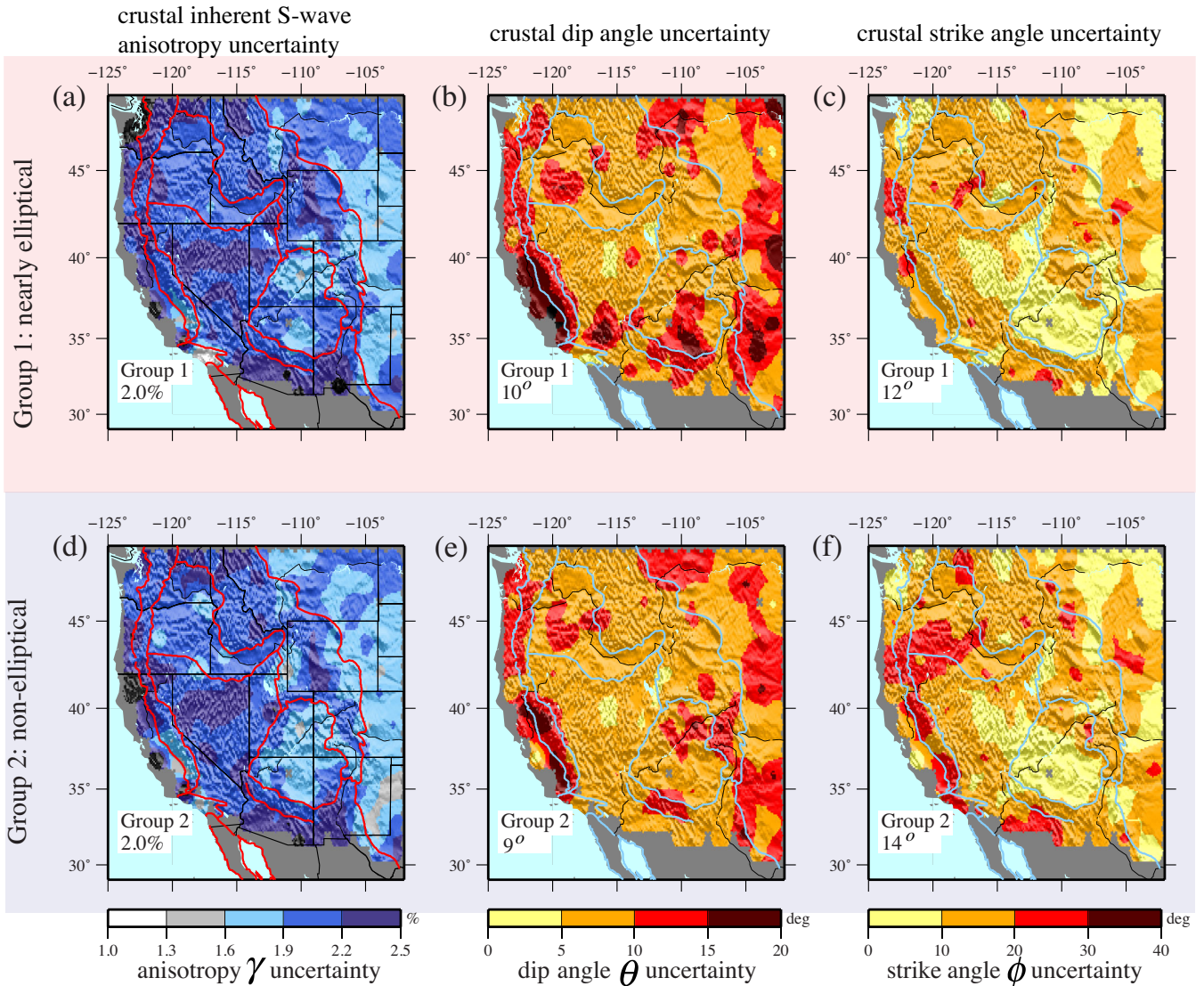


Figure 13. Local uncertainties for the model variables shown in Fig. 12. Average uncertainties across each map are inset.

4.8 per cent) than in Group 2 (6.6 ± 4.2 per cent). Group 1 models have nearly elliptical anisotropy, so $\delta \approx \varepsilon$. Thus, for Group 1 models, δ is on average larger (8.5 ± 6.7 per cent) than for Group 2 models (2.8 ± 5.3 per cent). For Group 2 models $\delta \ll \varepsilon$, on average.

6.2 On the cause of the bifurcation in strike angle of crustal anisotropy

The fact that two groups of solutions with orthogonal strike angles both fit the crustal sensitive Rayleigh wave data may be explained in terms of the phase speed surface produced by different elastic tensors. The phase speed surface can be computed by solving the Christoffel equation. For waves traveling in any direction, there are always three mutually orthogonal wave solutions, one (quasi-) P wave and two (quasi-) S waves. Normally, the S wave with faster speed is called S_1 , and the slower one is called S_2 . Note that S_1 and S_2 should not be associated with SV or SH waves, because S_1 and S_2 are defined based on the wave speed instead of the polarization direction. The discussion below only aims to provide a qualitative understanding of the bifurcation. For more insight, more sophisti-

cated forward computations would be required, which is beyond the scope of this paper.

Fig. 15 shows the phase speed surface of P , S_1 and S_2 waves, together with the polarization direction of the S_1 wave for two tilted elastic tensors with hexagonal symmetry, one is elliptical with a dip angle of 20° and strike angle of 210° , the other is non-elliptical with dip angle 20° and a strike angle 300° . Each surface plots a particular speed (V_{S_1} , V_{S_2} and P) for waves propagating in different directions. Each panel is a lower hemisphere plot so that horizontally propagating waves (surface waves) are sensitive to wave speeds at the edge of the diagram. These two tensors represent our Group 1 and Group 2 models that have different ellipticity of anisotropy and orthogonal strike angles. The most prominent feature of the non-elliptical (Group 2) tensor is that the polarization direction of the S_1 wave suddenly changes from radial to tangential at some degree oblique to the symmetry axis. A Rayleigh wave that is propagating horizontally in a hexagonally symmetric medium with a shallow to moderate dip is mainly sensitive to the phase speed of the S_2 wave (V_{S_2}). In the following paragraphs, therefore, we will concentrate discussion on the speed V_{S_2} . We will demonstrate that the two groups of elastic

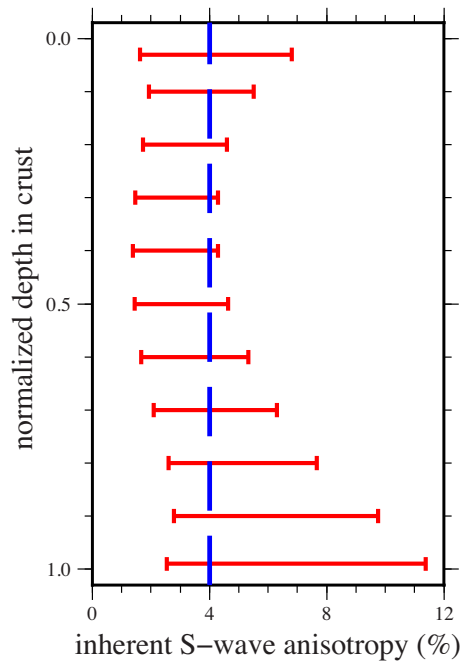


Figure 14. The spatially averaged inherent S -wave anisotropy (γ) as a function of depth in the crust, where depth is normalized by local crustal thickness. The middle of the error bar is the average value of γ , in per cent, and the half width of the error bar is the spatial average of the one-standard deviation uncertainty. The blue dashed line indicates 4 per cent anisotropy, which is the amplitude of anisotropy averaged over the whole crystalline crust and over the study region.

tensors produce the same azimuthal pattern in wave speed V_{S_2} even though their strikes angles differ by 90° .

In an elliptically hexagonally symmetric anisotropic medium (Group 1), the V_{S_2} surface has its minimum value oblique to the symmetry axis. In a non-elliptical hexagonal material, the pattern of the V_{S_2} surface is reversed: V_{S_2} has its maximum value oblique to the symmetry axis. Because horizontally propagating Rayleigh waves only sample the outer margin of the wave speed surface, we plot the value of V_{S_2} at the edge of the surface as a function of azimuth (Fig. 16a). We find that despite the orthogonal strike directions, the two groups of models produce similar azimuthal patterns of V_{S_2} , with the same fast axis directions. Group 1 models have their V_{S_2} fast axis direction parallel to the strike angle of the elastic tensor, whereas Group 2 models have their fast axis directions orthogonal to the strike. This phenomenon results in the same fast direction for the Rayleigh waves, even when the orientation of the inherent elastic tensor is different. These results highlight the fact that the fast direction of Rayleigh wave is not necessarily parallel to the strike of anisotropy, but depends on a property of the medium, whether the anisotropy is elliptical or not. This phenomenon is similar to what Song & Kawakatsu (2012) found for shear wave splitting.

In contrast with the propagation of S_2 waves, however, a horizontally propagating P wave is always fastest parallel to the strike of a dipping hexagonally symmetric elastic tensor (Fig. 16b). Therefore, a P wave's fast direction always indicates the strike direction.

In conclusion, for both groups of models the Rayleigh wave fast axis direction is the same even though the strike of the anisotropy differs by 90° . However, the P wave fast directions in the two groups will be orthogonal to each other, consistent with a 90° rotation of the strike. Therefore, observations of P wave anisotropy provide

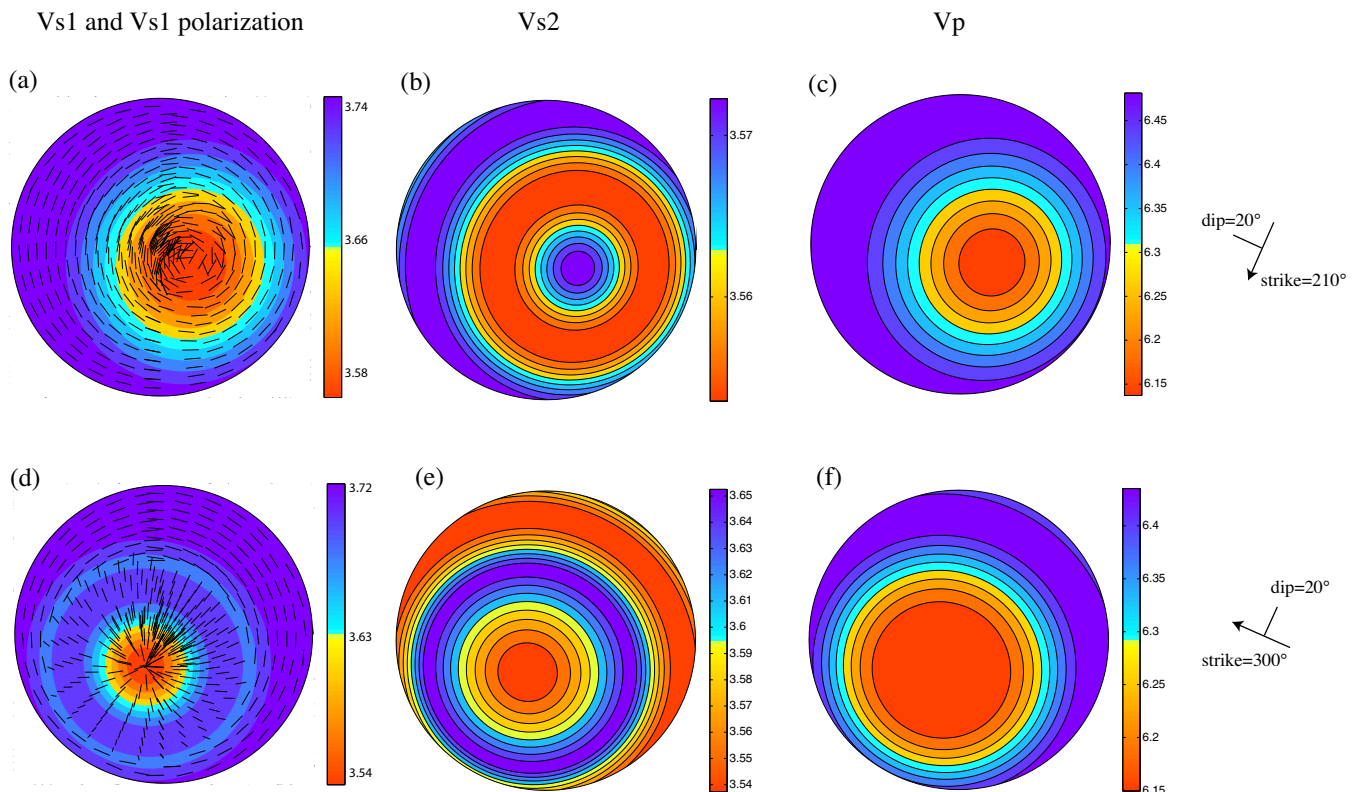


Figure 15. Phase velocity surfaces (lower hemisphere) of V_{s_1} , V_{s_2} and V_p for two elastic tensors with hexagonal symmetry: one is elliptical (a–c, represents a Group 1 model) and the other one is non-elliptical (d–f, represents a Group 2 model). V_{s_1} polarizations are indicated in (a) and (c) where the black bars are the projection of the V_{s_1} vector onto the plane of stereonet. The orientations of the two elastic tensor groups are shown at the right hand side of the figure.

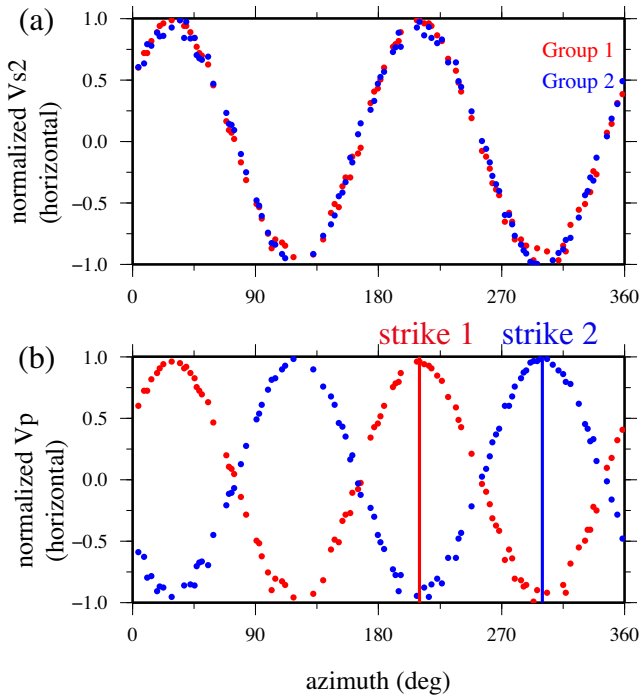


Figure 16. Azimuthal velocity variations of the horizontally propagating (a) S_2 wave and (b) P wave where all the velocities are normalized. The red and blue dots represent the velocities computed from the elastic tensor of Group 1 and Group 2, respectively (the velocities at the edge of Figs 15b and d). The vertical lines in (b) indicate the strike direction, red for Group 1 and blue for Group 2.

unambiguous information about the orientation of the strike angle of anisotropy, but Rayleigh wave traveltimes do not. In addition, observations from waves with near-vertical incidence angles, such as receiver functions (e.g. Levin & Park 1997; Savage 1998; Bianchi *et al.* 2008, 2010; Liu & Niu 2012; Schulte-Pelkum & Mahan 2014a,b), may also provide unambiguous information about the orientation of the strike angle of anisotropy.

6.3 The strike angle of crustal anisotropy and the Rayleigh wave fast axis direction

As discussed in Section 5 and earlier in this section, the posterior distribution divides into two disjoint groups of crustal models according to the estimated strike angle (ϕ) of anisotropy, which is defined in Fig. 1(a). The physical cause of this bifurcation is discussed in Section 6.2. Thus, at each spatial grid point there are two distinct distributions of elastic tensors and orientations (or tilts) that fit the Rayleigh wave azimuthal anisotropy observations approximately equally well. For Group 1, the set of models with approximately elliptical anisotropy ($\varepsilon \approx \delta$) and typically larger value of η , the distribution of strike angles is shown in Fig. 12(c). These strike angles are very similar to the Rayleigh wave fast axis directions for waves that sample the crust (e.g. 10–20 s period, Fig. 4a). Fig. 17 illustrates this fact by plotting as blue dots the 16 s period Rayleigh wave fast axis directions against the Group 1 strike angles (ϕ_1) at each location. The mean and standard deviation of the difference are 0.2° and 21.0° , respectively. The geographical distribution of the strike angles (and fast axis directions for crustal sensitive Rayleigh waves) are similar to those found by Lin *et al.* (2011), who discuss the geological coherence of the observations, so we forgo this discussion here.

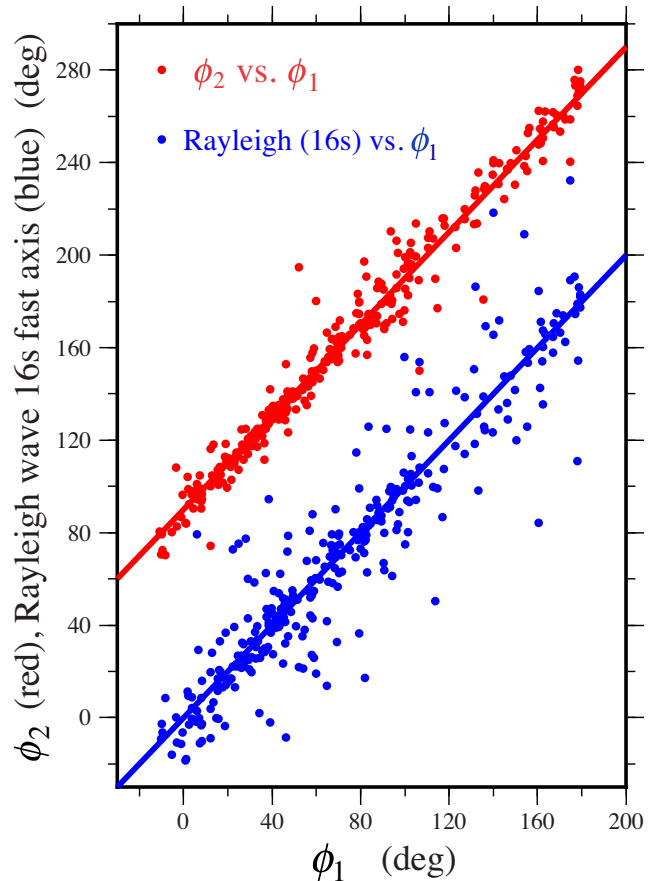


Figure 17. (Red dots) Comparison between the Group 2 strike angle (ϕ_2) and the Group 1 strike angle (ϕ_1) across the study region, where the red line represents $y = x + 90^\circ$. The strike angles in the two groups are approximately orthogonal. (Blue dots) Comparison between the fast azimuth of the Rayleigh wave at 16 s period to the Group 1 strike angle, where the blue line represents $y = x$. Crustal sensitive Rayleigh wave fast axis directions are approximately parallel to Group 1 strike directions and perpendicular to Group 2 strike directions.

The second group of models, Group 2, possesses strike angles that are distinct from Group 1, ε is typically significantly larger than δ , so the anisotropy is decidedly non-elliptical and η is usually smaller than 0.8. As Fig. 17 also shows with red symbols, the strike angles of Group 2 (ϕ_2) are, on average, perpendicular to the strike angles of Group 1 (ϕ_1) such that the average angular difference and standard deviation are 90.2° and 8.8° , respectively. This distribution is tighter than the comparison with Rayleigh wave fast axis directions because Rayleigh wave fast axes at a particular period are measurements and are, therefore, noisy.

In summary, Rayleigh wave fast axis directions are ambiguously related to the strike of inherent crustal anisotropy. In fact, the fast axis direction will only parallel the strike direction if the crustal anisotropy is largely elliptical in nature. As petrological information has grown concerning the seismic anisotropy in the crust, evidence has mounted that crustal anisotropy is probably not strongly elliptical (e.g. Tatham *et al.* 2008; Brownlee *et al.* 2011; Erdman *et al.* 2013). Thus, the geologically favoured models are probably from Group 2. Therefore, crustal sensitive Rayleigh waves must only be used with caution to reveal the orientation of the geological features that are causing the anisotropy. It is probably more likely for the fast axis direction of crustal sensitive Rayleigh waves to point

perpendicular to the strike direction than parallel to it. Similarly, assuming nearly vertical shear waves, crustal shear wave splitting will have its fast axis in the direction of the Rayleigh-wave fast axis. Therefore, the fast splitting direction of crustal SKS is also more likely to point perpendicular to the strike direction than parallel to it.

To recover unambiguous information about the strike angle, other types of data need to be introduced. As discussed in Section 6.2, observations of crustal P -wave anisotropy can resolve the ambiguity because the P wave fast direction is always parallel to the strike direction as can observations of anisotropy using receiver functions. Admittedly, however, these are difficult observations to make.

6.4 On the interpretation of the inferred dip angle

There are two alternative interpretations of the inferred dip angle, θ : that it is a measurement of the actual geometry of the foliation plane of material composing the crust or that it is a proxy for another potentially unknown non-geometric variable. We will first discuss the latter alternative.

First, it is possible that the observed dip angle is proxy for other variables. Even though our models are expressed in terms of a tilted hexagonally symmetric medium, crustal anisotropy may not actually be hexagonally symmetric, or the approximation to hexagonal symmetry may not be accurate everywhere. Crustal anisotropy may indeed possess lower order symmetry than hexagonal. Tilting a material can have the effect of decreasing the apparent symmetry of the material if viewed in the same coordinate system (Okaya & McEvilly 2003). In principle, therefore, a lower order of symmetry could be approximated by a higher order of symmetry (e.g. hexagonally symmetric) through tilting. It is possible that the efficacy of this approximation is enhanced by the fact that surface wave travel-time data are insensitive to 8 of the 21 moduli that constitute a general elastic tensor (the Appendix). It is conceivable, therefore, that the effect on our data that we interpret as a tilt (non-zero dip angle) could have resulted from the non-hexagonal component of the actual elastic tensor of the medium. What we would estimate in this case is an ‘apparent dip angle’ that is proxy for the extent to which the medium deviates from hexagonal symmetry.

We have experimented with numerically fitting tilted hexagonally symmetric elastic tensors to nearly orthorhombic tensors from crustal rock samples (Tatham *et al.* 2008; Brownlee *et al.* 2011; Erdman *et al.* 2013) using only the 11 combinations to which observations of the 2ψ component of Rayleigh wave and the azimuthally isotropic Rayleigh and Love wave data are sensitive (the Appendix). We estimate an apparent dip angle that measures the medium’s deviation from hexagonal symmetry. Apparent dip angles resulting from this fit typically range between 15° and 25° . The dip angles that we infer, therefore, may be a result of approximating orthorhombic or other lower-symmetry material with hexagonally symmetric tensors, in which case steeper dip angles would reflect a greater deviation from hexagonal symmetry.

Secondly, there is also likely to be at least some component of the inferred crustal elastic tensors related to the actual dip of the foliation of the material. In fact, variations in observed dip angles make geologic sense in some regions. For example, observed dips are shallow beneath the Basin and Range province, which is consistent with large-scale crustal extension along low-angle normal faults and horizontal detachment faults (e.g. Xiao *et al.* 1991; Johnson & Loy 1992; John & Foster 1993; Malavieille 1993). The steeper dip angles observed in California are also consistent with a lower crust consisting of foliated Pelona-Orocopia-Rand schist (e.g.

Jacobson 1983; Jacobson *et al.* 2007; Chapman *et al.* 2010), which was underplated during Laramide flat-slab subduction (e.g. Jacobson *et al.* 2007). In other regions, such as beneath the Colorado Plateau, the potential geologic meaning of the steeper observed dip angles is less clear; perhaps the steeper dips are an indication of a change in crustal composition resulting in an elastic tensor with low symmetry.

6.5 Comparison with previous studies: inherent versus apparent anisotropy

A tilted hexagonally symmetric elastic tensor will generate both apparent radial and azimuthal anisotropy in surface waves as demonstrated by Fig. 1(b). At a given depth, referencing the notation in the Appendix, we define apparent S -wave radial anisotropy as:

$$\hat{\gamma} = (\hat{N} - \hat{L})/2\hat{L}, \quad (9)$$

where

$$\hat{N} = (C_{11} + C_{22})/8 - C_{12}/4 + C_{66}/2 \quad \hat{L} = (C_{44} + C_{55})/2, \quad (10)$$

We also define the amplitude of apparent SV-wave azimuthal anisotropy as:

$$|G|/L = \sqrt{G_c^2 + G_s^2}/L, \quad (11)$$

where

$$G_c = (\delta C_{55} - \delta C_{44})/2 = (C_{55} - C_{44})/2 \quad (12)$$

$$G_s = \delta C_{45} = C_{45}. \quad (13)$$

The components of the modulus matrix, $C_{\alpha\beta}$, are functions of the inherent elastic moduli (A, C, N, L, F) and tilt (θ, ϕ). The strength of inherent S -wave anisotropy is defined by eq. (5).

As shown in Fig. 1(b), when the inherent elastic moduli (A, C, N, L, F) are fixed, variations in dip angle θ produce the variations in the apparent anisotropies. The amplitudes of apparent anisotropies are always smaller than the inherent anisotropy except for two extreme cases, $\theta = 0^\circ$ and $\theta = 90^\circ$. Thus, if Earth structure has $\theta \in (0^\circ, 90^\circ)$, then neither apparent radial nor apparent azimuthal anisotropy will reflect the real strength of anisotropy (inherent anisotropy) in the Earth.

In studies of anisotropy based either on isotropic dispersion curves or azimuthally anisotropic dispersion curves alone, it is the apparent anisotropy instead of the inherent anisotropy that is estimated. For example, in studies of radial anisotropy using surface waves (e.g. Moschetti *et al.* 2010a,b; Xie *et al.* 2013), only the azimuthally isotropic Rayleigh and Love wave dispersion curves are used to produce a transversely isotropic model, which produces no azimuthal anisotropy. Because the azimuthally isotropic dispersion curves are only sensitive to the effective transversely isotropic part of the elastic tensor ($\hat{A}, \hat{C}, \hat{N}, \hat{L}, \hat{F}$, the Appendix), this transversely isotropic model is the effective transversely isotropic (ETI) part of our model. To prove this, we compute the ETI part of our model, from which the apparent S -wave radial anisotropy can be generated (Fig. 18). The apparent S -wave radial anisotropy for both Group 1 and Group 2 models are very similar to each other, they both change appreciably across the study region, with large amplitudes in the Basin and Range province and small amplitudes in the Colorado Plateau. This pattern is very similar to that observed by Moschetti *et al.* (2010b), and thus demonstrates that inversion

crustal apparent S-wave radial anisotropy

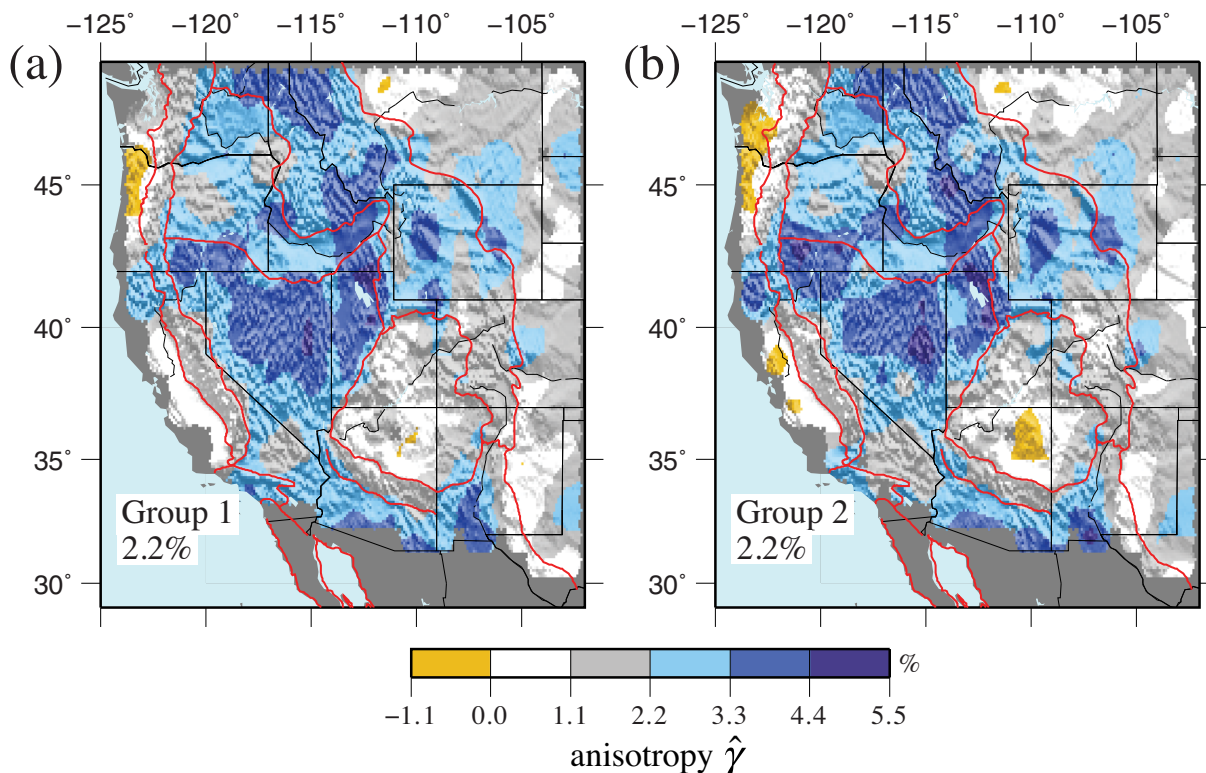


Figure 18. The mean of the posterior distribution of apparent S -wave radial anisotropy, $\hat{\gamma}$, averaged vertically across the crust for (a) Group 1 models and (b) Group 2 models. Average values across the crust and region of study are inset.

with isotropic dispersion curves alone results in observations of apparent S -wave radial anisotropy, $\hat{\gamma}$. Similarly, inversion with azimuthally anisotropic dispersion curves alone results in apparent quasi-SV-wave azimuthal anisotropy (e.g. Lin *et al.* 2011).

The apparent radial and apparent azimuthal anisotropy reflect different aspects of the inherent elastic tensor and both mix information from the inherent elastic moduli and the orientation. As described in Section 6.1, the amplitude of γ , the inherent S -wave anisotropy, does not change strongly across the region, and averages about 4 per cent. In contrast, the amplitude of $\hat{\gamma}$, the apparent radial anisotropy, changes strongly across the region in a pattern similar to the variation of the dip angle θ , and averages to about 2 per cent. Thus, the lateral variation of $\hat{\gamma}$ results mainly from the variation of θ , and does not reflect the strength of γ .

In most surface wave studies, only the apparent anisotropies are estimated. Therefore, the results depend on the unknown orientation of the medium (or the non-hexagonality of medium for which the dip angle may be a proxy), which limits their usefulness to constrain the elastic properties of the medium (e.g. the inherent S -wave anisotropy, γ).

6.6 Mantle anisotropy across the western United States

Although the focus of this paper is on crustal anisotropy we present here a brief discussion of the mantle anisotropy that emerges from the inversion. Fig. 19 shows the prior and posterior distributions at 60 km depth at point A in the Basin and Range province. At this point, the mean of the posterior distribution is between 4 and

5 per cent for both inherent S -wave (γ) and P -wave (ε) anisotropy, both the dip and strike angles are fairly well resolved with a mean dip angle of $27^\circ (\pm 7^\circ)$ and strike angle of $66^\circ (\pm 8^\circ)$, the mean of the posterior distribution for η is $0.96 (\pm 0.04)$ which is much higher than in the crust, and the anisotropy is indistinguishable from elliptical ($\varepsilon - \delta = -0.04 \pm 0.06$). The nearly elliptical nature of mantle anisotropy is also quite different from what we observe in the crust. This location is fairly typical of mantle anisotropy across the western United States, as γ averages 4.4 per cent (± 2.6 per cent) across the western United States with an average dip angle of $21^\circ (\pm 8^\circ)$. We note in passing that such a steep dip angle may result from a strong orthorhombic component to the mantle elastic tensors and may not result from the actual tilt of the medium. Because, unlike the crust, the posterior distribution in the mantle does not bifurcate according to strike angle, Rayleigh wave fast axis directions are unambiguously related to the strike angle in the mantle. Because mantle anisotropy is nearly elliptical (with η close to one), Rayleigh wave fast axes actually align with the strike angle rather than orthogonal to it. However, mantle strike angle is not everywhere well determined across the region as the average uncertainty is nearly 30° . The inability to resolve mantle strike angle unambiguously across the region with the current data set and method is one of the reasons we focus interpretation on crustal anisotropy here and we plan to return to mantle anisotropy in a later contribution.

7 SUMMARY AND CONCLUSIONS

The motivation for this paper is to present a method of inversion that explains surface wave observations of both radial and azimuthal

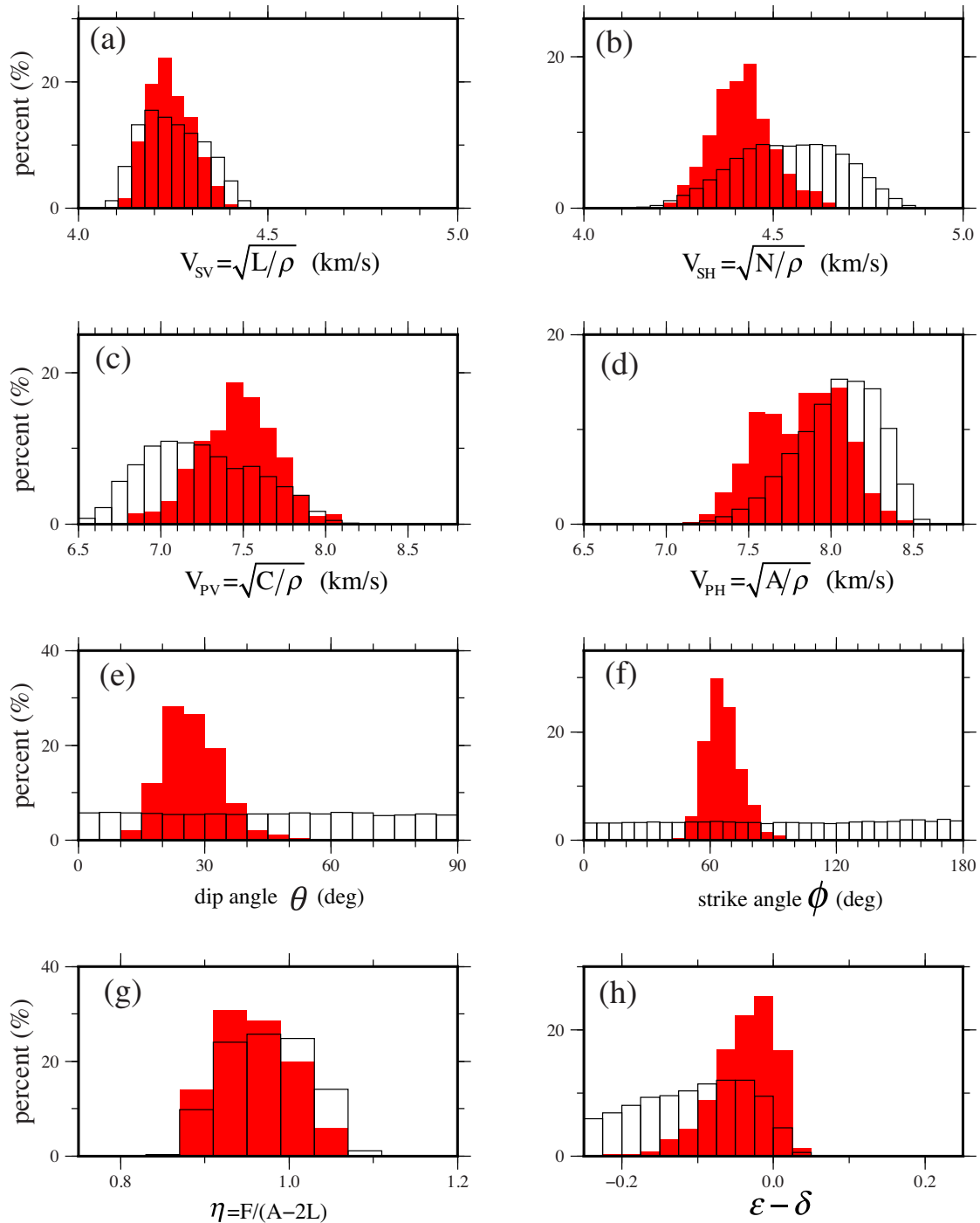


Figure 19. Prior and posterior distributions for several model parameters in the mantle at 60 km depth for Point A (in Basin and Range, identified in Fig. 3a). Similar to Fig. 8, white histograms indicate the prior distributions and red histograms represent the posterior distributions. Posterior distributions in the mantle are not bimodal as they are in the crust.

anisotropy, which are seldom explained simultaneously. The method we present here inverts for the inherent properties of the medium represented by a hexagonally symmetric elastic tensor, with an arbitrarily oriented symmetry axis, which we refer to as ‘tilted’. The elastic tensor itself at each depth is given by five elastic moduli (A , C , N , L and F or η) and the tilt is defined by two rotation angles: the dip and strike, which are illustrated in Fig. 1(a). We refer to these moduli as ‘inherent’, as they reflect the characteristics of the elastic tensor irrespective of its orientation.

We show that observations of radial anisotropy and the 2ψ component of azimuthal anisotropy for Rayleigh waves obtained using USArray in the western United States can be fit well by tilted hexagonally symmetric elastic tensors in the crust and mantle, subject to the constraints listed in the text. The inversion that we apply is a Bayesian Monte Carlo method, which yields a posterior distribution that reflects both the data and prior constraints. The most noteworthy constraint is that the tilt angles (dip, strike) are constant in the crust and mantle, but may differ between the crust and mantle.

The results are summarized as posterior distributions of smoothly depth-varying inherent (unrotated) moduli (A or V_{PH} , C or V_{PV} , N or V_{SH} , L or V_{SV} and F or η) as well as dip and strike angles. The standard deviation of the posterior distribution defines the uncertainties in these quantities. Anisotropy can be summarized with the Thomsen parameters, inherent S -wave anisotropy (γ) and inherent P -wave anisotropy (ε), and either η or δ (which is the third Thomsen parameter).

Because the crust is constrained by the data better than the mantle and γ (inherent S -wave anisotropy) is determined more tightly than ε (inherent P -wave anisotropy), we focus interpretation on γ in the crust as well as the tilt angles. Major results include the following. (1) γ is fairly homogeneous vertically across the crust, on average, and spatially across the western United States. (2) Averaging over the region of study and in depth, γ in the crust is approximately 4 ± 2 per cent. (3) Crustal strike angles (ϕ) in the posterior distributions bifurcate into two sets of models that we refer to as Groups 1 and 2. Models in Group 1 have strike angles that approximately parallel crust-sensitive Rayleigh wave fast axis directions, and typically have larger values of η and nearly elliptical anisotropy ($\varepsilon \approx \delta$). Group 2 models have strike angles that are approximately orthogonal to crust-sensitive Rayleigh wave fast directions, smaller values of η , and more strongly non-elliptical anisotropy where typically $\varepsilon > \delta$. Mantle strike angles do not bifurcate as they do in the crust because of tighter constraints imposed on η in the inversion. (4) γ in the crust is approximately the same in the two groups of models. (5) Dip angles in the two groups of models vary spatially in similar ways and display geological coherence; for example, they are smaller in the Basin and Range province than in the Colorado Plateau or the Great Plains. However, in Group 1 they are slightly larger than in Group 2, averaging $30^\circ \pm 10^\circ$ in Group 1 and $25^\circ \pm 9^\circ$ in Group 2. (6) Rayleigh wave fast axis directions are ambiguously related to the strike of anisotropy, but recent studies of the anisotropy of crustal rocks (e.g. Tatham *et al.* 2008; Brownlee *et al.* 2011; Erdman *et al.* 2013) imply that the crustal anisotropy is probably not nearly elliptical, which favours Group 2 models. Therefore, under the assumption that crustal anisotropy is approximately hexagonally symmetric with an arbitrary tilt, Rayleigh wave fast axis directions for crustal sensitive Rayleigh waves will be oriented orthogonal rather than parallel to the strike of anisotropy. Interpretation of Rayleigh wave fast axis directions in terms of crustal structure must be performed with caution. (7) The estimated dip angle may be interpreted in two alternative ways. It is either an actual measure of the dip of the foliation plane of anisotropic material within the crust, or it is proxy for another non-geometric variable, most likely a measure of the deviation from hexagonal symmetry of the medium. (8) By attempting to estimate the inherent moduli that compose the elastic tensor of the crust (and mantle), our approach differs from earlier studies that produce measurements of ‘apparent’ moduli. Because tilting a medium produces apparent radial and apparent azimuthal anisotropies that are both smaller than the inherent anisotropy in amplitude, previous studies have tended to underestimate the strength of anisotropy.

In the future, we intend to improve long period data in order to produce improved results for the mantle and apply the method more generally to observations of surface wave anisotropy in the United States and elsewhere. It will also be desirable to apply increasingly strong constraints on allowed anisotropy and continue to revise the interpretation of results as more information accrues about crustal anisotropy from laboratory measurements on crustal rocks. In particular, it may make sense to experiment with more general theoretical models of anisotropy in the inversion, perhaps

by considering a mixture of elastic tensors with hexagonal and orthorhombic symmetry. Ultimately, we aim to interpret the results in terms of petrological models that agree with the inferred elastic tensor.

ACKNOWLEDGEMENTS

The authors are grateful to Don Anderson, Peter Molnar, Jean-Paul Montagner and David Okaya for helping to inspire and motivate this work. They also thank Craig Jones and Vera Schulte-Pelkum for comments on an early draft of this paper, Jean-Paul Montagner and an anonymous reviewer for comments that helped to improve the paper, and Leon Thomsen for valuable conversations. The facilities of the IRIS Data Management System, and specifically the IRIS Data Management Center, were used to access the waveform and metadata required in this study. The IRIS DMS is funded through the National Science Foundation and specifically the GEO Directorate through the Instrumentation and Facilities Program of the National Science Foundation under Cooperative Agreement EAR-0552316. This work utilized the Janus supercomputer, which is supported by the National Science Foundation (award number CNS-0821794) and the University of Colorado Boulder. The Janus supercomputer is a joint effort of the University of Colorado Boulder, the University of Colorado Denver and the National Center for Atmospheric Research. Aspects of this research were supported by NSF grants EAR-1252085 and EAR-1246925 at the University of Colorado at Boulder.

REFERENCES

- Anderson, D.L. & Regan, J., 1983. Upper mantle anisotropy and the oceanic lithosphere, *Geophys. Res. Lett.*, **10**(9), 841–844.
- Anderson, D.L., Minster, B. & Cole, D., 1974. The effect of oriented cracks on seismic velocities, *J. geophys. Res.*, **79**(26), 4011–4015.
- Auld, B.A., 1973. *Acoustic Fields and Waves in Solids*, Vol. I, p. 423, Wiley.
- Babuška, V., 1991. *Seismic Anisotropy in the Earth, Modern Approaches in Geophysics*, Vol. 10, Kluwer Academic Publishers.
- Backus, G.E., 1962. Long-wave elastic anisotropy produced by horizontal layering, *J. geophys. Res.*, **67**(11), 4427–4440.
- Bensen, G.D., Ritzwoller, M.H. & Yang, Y., 2009. A 3-D shear velocity model of the crust and uppermost mantle beneath the United States from ambient seismic noise, *Geophys. J. Int.*, **177**(3), 1177–1196.
- Bianchi, I., Piana Agostinetti, N., De Gori, P. & Chiarabba, C., 2008. Deep structure of the Colli Albani volcanic district (central Italy) from receiver functions analysis, *J. geophys. Res.: Solid Earth*, **113**(B9), B09313, doi:10.1029/2007JB005548.
- Bianchi, I., Park, J., Piana Agostinetti, N. & Levin, V., 2010. Mapping seismic anisotropy using harmonic decomposition of receiver functions: an application to Northern Apennines, Italy, *J. geophys. Res.: Solid Earth*, **115**(B12), B12317, doi:10.1029/2009JB007061.
- Brocher, T.M., 2005. Empirical relations between elastic wavespeeds and density in the Earth’s crust, *Bull. seism. Soc. Am.*, **95**(6), 2081–2092.
- Brownlee, S.J., Hacker, B.R., Salisbury, M., Seward, G., Little, T.A., Baldwin, S.L. & Abers, G.A., 2011. Predicted velocity and density structure of the exhuming Papua New Guinea ultrahigh-pressure terrane, *J. geophys. Res.: Solid Earth*, **116**(B8), B08206, doi:10.1029/2011JB008195.
- Buehler, J.S. & Shearer, P.M., 2014. Anisotropy and V_p/V_s in the uppermost mantle beneath the western United States from joint analysis of Pn and Sn phases, *J. geophys. Res.*, **119**(2), 1200–1219.
- Burgos, G., Montagner, J.-P., Beucler, E., Capdeville, Y., Mocquet, A. & Drilleau, M., 2014. Oceanic lithosphere-asthenosphere boundary from surface wave dispersion data, *J. geophys. Res.: Solid Earth*, **119**(2), 1079–1093.
- Carcione, J.J.M., 2007. *Wave Fields in Real Media: Wave Propagation in Anisotropic, Anelastic, Porous and Electromagnetic Media*, Elsevier.

- Chapman, A.D., Kidder, S., Saleeby, J.B. & Ducea, M.N., 2010. Role of extrusion of the Rand and Sierra de Salinas schists in Late Cretaceous extension and rotation of the southern Sierra Nevada and vicinity, *Tectonics*, **29**(5), TC5006, doi:10.1029/2009TC002597.
- Christensen, N.I., 1984. The magnitude, symmetry and origin of upper mantle anisotropy based on fabric analyses of ultramafic tectonites, *Geophys. J. Int.*, **76**(1), 89–111.
- Christensen, N.I., 1996. Poisson's ratio and crustal seismology, *J. geophys. Res.*, **101**(B2), 3139–3156.
- Christensen, N.I. & Mooney, W.D., 1995. Seismic velocity structure and composition of the continental crust: a global view, *J. geophys. Res.: Solid Earth*, **100**(B6), 9761–9788.
- Crampin, S., 1984. Effective anisotropic elastic constants for wave propagation through cracked solids, *Geophys. J. Int.*, **76**(1), 135–145.
- Dziewonski, A.M. & Anderson, D.L., 1981. Preliminary reference Earth model, *Phys. Earth planet. Inter.*, **25**(4), 297–356.
- Ekström, G., 2013. Love and Rayleigh phase-velocity maps, 5–40 s, of the western and central USA from USArray data, *Earth planet. Sci. Lett.*, **402**, 42–49.
- Ekström, G. & Dziewonski, A.M., 1998. The unique anisotropy of the Pacific upper mantle, *Nature*, **394**(6689), 168–172.
- Erdman, M.E., Hacker, B.R., Zandt, G. & Seward, G., 2013. Seismic anisotropy of the crust: electron-backscatter diffraction measurements from the Basin and Range, *Geophys. J. Int.*, **195**(2), 1211–1229.
- Forsyth, D.W., 1975. The early structural evolution and anisotropy of the oceanic upper mantle, *Geophys. J. Int.*, **43**(1), 103–162.
- Gung, Y., Panning, M. & Romanowicz, B., 2003. Global anisotropy and the thickness of continents, *Nature*, **422**(6933), 707–711.
- Hacker, B.R., Ritzwoller, M.H. & Xie, J., 2014. Central Tibet has a partially melted, mica-bearing crust, *Tectonics*, **33**, doi:10.1002/2014TC003534.
- Helbig, K. & Thomsen, L., 2005. 75-plus years of anisotropy in exploration and reservoir seismics: a historical review of concepts and methods, *Geophysics*, **70**(6), 9ND–23ND.
- Huang, H., Yao, H. & van der Hilst, R.D., 2010. Radial anisotropy in the crust of SE Tibet and SW China from ambient noise interferometry, *Geophys. Res. Lett.*, **37**, doi:10.1029/2010GL044981.
- Jacobson, C.E., 1983. Structural geology of the Pelona Schist and Vincent thrust, San Gabriel Mountains, California, *Geol. Soc. Am. Bull.*, **94**(6), 753–767.
- Jacobson, C.E., Grove, M., Vucic, A., Pedrick, J.N. & Ebert, K.A., 2007. Exhumation of the Orcopia Schist and associated rocks of southeastern California: relative roles of erosion, syn-subduction tectonic denudation, and middle Cenozoic extension, *Geol. Soc. Am. Spec. Paper*, **419**, 1–37.
- Jaxybulatov, K., Shapiro, N.M., Koulakov, I., Mordret, A., Landès, M. & Sens-Schönfelder, C., 2014. A large magmatic sill complex beneath the Toba caldera, *Science*, **346**(6209), 617–619.
- John, B.E. & Foster, D.A., 1993. Structural and thermal constraints on the initiation angle of detachment faulting in the southern Basin and Range: the Chemehuevi Mountains case study, *Geol. Soc. Am. Bull.*, **105**(8), 1091–1108.
- Johnson, R.A. & Loy, K.L., 1992. Seismic reflection evidence for seismogenic low-angle faulting in southeastern Arizona, *Geology*, **20**(7), 597–600.
- Kawakatsu, H., Kumar, P., Takei, Y., Shinohara, M., Kanazawa, T., Araki, E. & Suyehiro, K., 2009. Seismic evidence for sharp lithosphere-asthenosphere boundaries of oceanic plates, *Science*, **324**(5926), 499–502.
- Kennett, B.L.N., Engdahl, E.R. & Buland, R., 1995. Constraints on seismic velocities in the Earth from traveltimes, *Geophys. J. Int.*, **122**(1), 108–124.
- Kustowski, B., Ekström, G. & Dziewonski, A.M., 2008. Anisotropic shear-wave velocity structure of the Earth's mantle: a global model, *J. geophys. Res.: Solid Earth*, **113**(B6), B06306, doi:10.1029/2007JB005169.
- Levin, V. & Park, J., 1997. Crustal anisotropy in the Ural Mountains Foredeep from teleseismic receiver functions, *Geophys. Res. Lett.*, **24**(11), 1283–1286.
- Lin, F.-C. & Ritzwoller, M.H., 2011. Helmholtz surface wave tomography for isotropic and azimuthally anisotropic structure, *Geophys. J. Int.*, **186**(3), 1104–1120.
- Lin, F.-C., Ritzwoller, M.H. & Snieder, R., 2009. Eikonal tomography: surface wave tomography by phase front tracking across a regional broadband seismic array, *Geophys. J. Int.*, **177**(3), 1091–1110.
- Lin, F.-C., Ritzwoller, M.H., Yang, Y., Moschetti, M.P. & Fouch, M.J., 2011. Complex and variable crustal and uppermost mantle seismic anisotropy in the western United States, *Nat. Geosci.*, **4**(1), 55–61.
- Lin, F.-C., Schmandt, B. & Tsai, V.C., 2012. Joint inversion of Rayleigh wave phase velocity and ellipticity using USArray: constraining velocity and density structure in the upper crust, *Geophys. Res. Lett.*, **39**(12), L12303, doi:10.1029/2012GL052196.
- Lin, F.-C., Tsai, V.C. & Schmandt, B., 2014. 3-D crustal structure of the western United States: application of Rayleigh-wave ellipticity extracted from noise cross-correlations, *Geophys. J. Int.*, **198**(2), 656–670.
- Liu, H. & Niu, F., 2012. Estimating crustal seismic anisotropy with a joint analysis of radial and transverse receiver function data, *Geophys. J. Int.*, **188**(1), 144–164.
- Lowry, A. R. & Pérez-Gussinyé, M., 2011. The role of crustal quartz in controlling Cordilleran deformation, *Nature*, **471**(7338), 353–357.
- Malavieille, J., 1993. Late Orogenic extension in mountain belts: insights from the basin and range and the Late Paleozoic Variscan Belt, *Tectonics*, **12**(5), 1115–1130.
- Marone, F. & Romanowicz, B., 2007. The depth distribution of azimuthal anisotropy in the continental upper mantle, *Nature*, **447**(7141), 198–201.
- Masters, G., Barmine, M.P. & Kientz, S., 2007. Mineos User's Manual, in Computational Infrastructure for Geodynamics, Calif. Inst. of Technol., Pasadena.
- Meissner, R., Rabbel, W. & Kern, H., 2006. Seismic lamination and anisotropy of the lower continental crust, *Tectonophysics*, **416**(1–4), 81–99.
- Montagner, J.-P. & Anderson, D.L., 1989. Constrained reference mantle model, *Phys. Earth planet. Inter.*, **58**(2–3), 205–227.
- Montagner, J.-P. & Jobert, N., 1988. Vectorial tomography—II. Application to the Indian Ocean, *Geophys. J.*, **94**(2), 309–344.
- Montagner, J.-P. & Nataf, H.-C., 1986. A simple method for inverting the azimuthal anisotropy of surface waves, *J. geophys. Res.*, **91**(B1), 511, doi:10.1029/JB091iB01p00511.
- Montagner, J.-P. & Nataf, H.-C., 1988. Vectorial tomography—I. Theory, *Geophys. J.*, **94**(2), 295–307.
- Moschetti, M.P., Ritzwoller, M.H., Lin, F.-C. & Yang, Y., 2010a. Crustal shear wave velocity structure of the western United States inferred from ambient seismic noise and earthquake data, *J. geophys. Res.*, **115**, doi:10.1029/2010JB007448.
- Moschetti, M.P., Ritzwoller, M.H., Lin, F. & Yang, Y., 2010b. Seismic evidence for widespread western-US deep-crustal deformation caused by extension, *Nature*, **464**(7290), 885–889.
- Nettles, M. & Dziewonski, A.M., 2008. Radially anisotropic shear velocity structure of the upper mantle globally and beneath North America, *J. geophys. Res.*, **113**, doi:10.1029/2006JB004819.
- Okaya, D.A. & Christensen, N.I., 2002. Anisotropic effects of non-axial seismic wave propagation in foliated crustal rocks, *Geophys. Res. Lett.*, **29**(11), 2-1–2-4.
- Okaya, D.A. & McEvilly, T.V., 2003. Elastic wave propagation in anisotropic crustal material possessing arbitrary internal tilt, *Geophys. J. Int.*, **153**(2), 344–358.
- Park, J. & Levin, V., 2002. Seismic anisotropy: tracing plate dynamics in the mantle, *Science*, **296**(5567), 485–489.
- Ribe, N.M., 1992. On the relation between seismic anisotropy and finite strain, *J. geophys. Res.: Solid Earth*, **97**(B6), 8737–8747.
- Ritzwoller, M.H., Lin, F.-C. & Shen, W., 2011. Ambient noise tomography with a large seismic array, *Comptes Rendus Geosci.*, **343**(8–9), 558–570.
- Savage, M.K., 1998. Lower crustal anisotropy or dipping boundaries? Effects on receiver functions and a case study in New Zealand, *J. geophys. Res.: Solid Earth*, **103**(B7), 15 069–15 087.
- Schulte-Pelkum, V. & Mahan, K.H., 2014a. A method for mapping crustal deformation and anisotropy with receiver functions and first results from USArray, *Earth planet. Sci. Lett.*, **402**, 221–233.
- Schulte-Pelkum, V. & Mahan, K.H., 2014b. Imaging faults and shear zones using receiver functions, *Pure appl. Geophys.*, **171**, 2967–2991.

- Shapiro, N.M., Campillo, M., Stehly, L. & Ritzwoller, M.H., 2005. High-resolution surface-wave tomography from ambient seismic noise, *Science*, **307**(5715), 1615–1618.
- Shen, W., Ritzwoller, M.H., Schulte-Pelkum, V. & Lin, F.-C., 2013a. Joint inversion of surface wave dispersion and receiver functions: a Bayesian Monte-Carlo approach, *Geophys. J. Int.*, **192**(2), 807–836.
- Shen, W., Ritzwoller, M.H. & Schulte-Pelkum, V., 2013b. A 3-D model of the crust and uppermost mantle beneath the Central and Western US by joint inversion of receiver functions and surface wave dispersion, *J. geophys. Res.: Solid Earth*, **118**(1), 262–276.
- Simons, F.J., Van Der Hilst, R.D., Montagner, J.-P. & Zielhuis, A., 2002. Multimode Rayleigh wave inversion for heterogeneity and azimuthal anisotropy of the Australian upper mantle, *Geophys. J. Int.*, **151**(3), 738–754.
- Smith, M.L. & Dahlen, F.A., 1973. The azimuthal dependence of Love and Rayleigh wave propagation in a slightly anisotropic medium, *J. geophys. Res.*, **78**(17), 3321–3333.
- Smith, D.B., Ritzwoller, M.H. & Shapiro, N.M., 2004. Stratification of anisotropy in the Pacific upper mantle, *J. geophys. Res.: Solid Earth*, **109**(B11), B11309, doi:10.1029/2004JB003200.
- Song, T.-R.A. & Kawakatsu, H., 2012. Subduction of oceanic asthenosphere: evidence from sub-slab seismic anisotropy, *Geophys. Res. Lett.*, **39**(17), L17301, doi:10.1029/2012GL052639.
- Tatham, D.J., Lloyd, G.E., Butler, R.W.H. & Casey, M., 2008. Amphibole and lower crustal seismic properties, *Earth planet. Sci. Lett.*, **267**(1–2), 118–128.
- Thomsen, L., 1986. Weak elastic anisotropy, *Geophysics*, **51**(10), 1954–1966.
- Thomsen, L. & Anderson, D.L., 2015. Weak elastic anisotropy in global seismology, in *The Don L. Anderson Tribute*, eds Foulger, G. et al., AGU and GSA, <http://www.mantleplumes.org/TopPages/TheDLABook.html>.
- Wang, N., Montagner, J.-P., Fichtner, A. & Capdeville, Y., 2013. Intrinsic versus extrinsic seismic anisotropy: the radial anisotropy in reference earth models, *Geophys. Res. Lett.*, **40**(16), 4284–4288.
- Weiss, T., Siegesmund, S., Rabbel, W., Bohlen, T. & Pohl, M., 1999. Seismic velocities and anisotropy of the lower continental crust: a review, *Pure appl. Geophys.*, **156**(1–2), 97–122.
- Xiao, H.-B., Dahlen, F.A. & Suppe, J., 1991. Mechanics of extensional wedges, *J. geophys. Res.: Solid Earth*, **96**(B6), 10 301–10 318.
- Xie, J., Ritzwoller, M.H., Shen, W., Yang, Y., Zheng, Y. & Zhou, L., 2013. Crustal radial anisotropy across Eastern Tibet and the Western Yangtze Craton, *J. geophys. Res.: Solid Earth*, **118**(8), 4226–4252.
- Yang, Y., Ritzwoller, M.H., Zheng, Y., Shen, W., Levshin, A.L. & Xie, Z., 2012. A synoptic view of the distribution and connectivity of the mid-crustal low velocity zone beneath Tibet, *J. geophys. Res.*, **117**, doi:10.1029/2011JB008810.
- Yao, H., Van Der Hilst, R.D. & De Hoop, M.V., 2006. Surface-wave array tomography in SE Tibet from ambient seismic noise and two-station analysis – I. Phase velocity maps, *Geophys. J. Int.*, **166**(2), 732–744.
- Yao, H., van der Hilst, R.D. & Montagner, J.-P., 2010. Heterogeneity and anisotropy of the lithosphere of SE Tibet from surface wave array tomography, *J. geophys. Res.*, **115**(B12), B12307, doi:10.1029/2009JB007142.
- Yu, Y. & Park, J., 1993. Upper mantle anisotropy and coupled-mode long-period surface waves, *Geophys. J. Int.*, **114**(3), 473–489.
- Yuan, H. & Romanowicz, B., 2010. Lithospheric layering in the North American craton, *Nature*, **466**(7310), 1063–1068.
- Yuan, H., Romanowicz, B., Fischer, K.M. & Abt, D., 2011. 3-D shear wave radially and azimuthally anisotropic velocity model of the North American upper mantle, *Geophys. J. Int.*, **184**(3), 1237–1260.
- Zhou, Y., Nolet, G., Dahlen, F.A. & Laske, G., 2006. Global upper-mantle structure from finite-frequency surface-wave tomography, *J. geophys. Res.: Solid Earth*, **111**(B4), B04304, doi:10.1029/2005JB003677.

APPENDIX: THE FORWARD PROBLEM: COMPUTATION OF PERIOD AND AZIMUTHALLY VARIABLE PHASE SPEEDS FOR AN ARBITRARILY ORIENTED HEXAGONALLY SYMMETRIC ELASTIC TENSOR

Given an elastic tensor that varies with depth at a given location, we seek to compute how Rayleigh and Love wave phase velocities change with period T and azimuth ψ . The code MINEOS (Masters *et al.* 2007) computes period dependent Rayleigh and Love wave phase speeds at high accuracy for a transversely isotropic medium; that is, a medium with hexagonal symmetry and a vertical symmetry axis. Instead, we are interested in a medium whose elastic properties are given by an elastic tensor for a hexagonally symmetric medium with an arbitrarily oriented symmetry axis.

First, let the moduli A , C , N , L and F represent the elastic tensor at a particular depth for a hexagonally symmetric medium with a vertical symmetry axis, given by eq. (1) in the Introduction. Four of the five moduli are directly related to P and S wave speeds for waves propagating perpendicular or parallel to the symmetry axis using the following relationships: $A = \rho V_{PH}^2$, $C = \rho V_{PV}^2$, $L = \rho V_{SV}^2$, $N = \rho V_{SH}^2$. Here, ρ is density, V_{PH} and V_{PV} are the speeds of P waves propagating horizontally and vertically respectively, V_{SV} is the speed of the S wave propagating horizontally and polarized vertically or propagating vertically and polarized horizontally and V_{SH} is the speed of the S wave that is propagating in a horizontal direction and polarized horizontally. The modulus $F = \eta(A - 2L)$ affects the speed of waves propagating oblique to the symmetry axis and controls the shape of the shear wave phase speed surface (Okaya & Christensen 2002). For an isotropic medium, $A = C$, $L = N$, $F = A - 2L$, $\eta = 1$.

Next, rotate the tensor in eq. (1) through the two angles, θ (the dip angle) and ϕ (the strike angle), defined in Fig. 1(a), to produce the modulus matrix $C_{\alpha\beta}(\theta, \phi)$. We refer to a general reorientation of the symmetry axis as a tilt, which is achieved by pre- and post-multiplying the elastic modulus matrix by the appropriate Bond rotation matrix and its transpose, respectively (e.g. Auld 1973; Carcione 2007), which act to rotate the fourth-order elasticity tensor appropriately. The order of the rotations matters because the rotation matrices do not commute: first a counter-clockwise rotation through angle θ around the x -axis is applied followed by a second counter-clockwise rotation through angle ϕ around the z -axis. The rotation can fill all components of the modulus matrix but will preserve its symmetry:

$$C_{\alpha\beta}(\theta, \phi) = \begin{bmatrix} C_{11} & C_{12} & C_{13} & C_{14} & C_{15} & C_{16} \\ C_{12} & C_{22} & C_{23} & C_{24} & C_{25} & C_{26} \\ C_{13} & C_{23} & C_{33} & C_{34} & C_{35} & C_{36} \\ C_{14} & C_{24} & C_{34} & C_{44} & C_{45} & C_{46} \\ C_{15} & C_{25} & C_{35} & C_{45} & C_{55} & C_{56} \\ C_{16} & C_{26} & C_{36} & C_{46} & C_{56} & C_{66} \end{bmatrix} \quad (\text{A1})$$

Montagner & Nataf (1986) showed that this modulus matrix may be decomposed into an effective transversely isotropic (azimuthally independent) part, $C_{\alpha\beta}^{ETI}$, and an azimuthally anisotropic part, $C_{\alpha\beta}^{AA}$, as follows:

$$C_{\alpha\beta}(\theta, \phi) = \begin{bmatrix} \hat{A} & \hat{A} - 2\hat{N} & \hat{F} & 0 & 0 & 0 \\ \hat{A} - 2\hat{N} & \hat{A} & \hat{F} & 0 & 0 & 0 \\ \hat{F} & \hat{F} & \hat{C} & 0 & 0 & 0 \\ 0 & 0 & 0 & \hat{L} & 0 & 0 \\ 0 & 0 & 0 & 0 & \hat{L} & 0 \\ 0 & 0 & 0 & 0 & 0 & \hat{N} \end{bmatrix} + \begin{bmatrix} \delta C_{11} & \delta C_{12} & \delta C_{13} & \delta C_{14} & \delta C_{15} & \delta C_{16} \\ \delta C_{12} & \delta C_{22} & \delta C_{23} & \delta C_{24} & \delta C_{25} & \delta C_{26} \\ \delta C_{13} & \delta C_{23} & \delta C_{33} & \delta C_{34} & \delta C_{35} & \delta C_{36} \\ \delta C_{14} & \delta C_{24} & \delta C_{34} & \delta C_{44} & \delta C_{45} & \delta C_{46} \\ \delta C_{15} & \delta C_{25} & \delta C_{35} & \delta C_{45} & \delta C_{55} & \delta C_{56} \\ \delta C_{16} & \delta C_{26} & \delta C_{36} & \delta C_{46} & \delta C_{56} & \delta C_{66} \end{bmatrix} \quad (\text{A2})$$

where $\hat{A} = 3(C_{11} + C_{22})/8 + C_{12}/4 + C_{66}/2$, $\hat{C} = C_{33}$, $\hat{N} = (C_{11} + C_{22})/8 - C_{12}/4 + C_{66}/2$, $\hat{L} = (C_{44} + C_{55})/2$ and $\hat{F} = (C_{13} + C_{23})/2$

Eqs (1) and (A2) present a clear definition of what we call the ‘inherent’ and ‘apparent’ elastic moduli, respectively. The inherent moduli are A, C, N, L, F from the elastic tensor with a vertical symmetry axis and the apparent moduli are $\hat{A}, \hat{C}, \hat{N}, \hat{L}, \hat{F}$ from the effective transversely isotropic part of the rotated elastic tensor.

We seek expressions for the period dependence of the phase speed for both Rayleigh and Love waves as well as the 2ψ azimuthal dependence for Rayleigh waves because these are the observations we make. This computation is based on the introduction of a transversely isotropic reference elasticity tensor composed of the depth dependent reference moduli A_0, C_0, N_0, L_0, F_0 . The code MINEOS will compute Rayleigh and Love wave phase speed curves for the reference model [$c_0^R(T), c_0^L(T)$]. Then we define the effective transversely isotropic moduli relative to this reference:

$$\hat{A} = A_0 + \delta\hat{A}, \quad \hat{C} = C_0 + \delta\hat{C}, \quad \hat{N} = N_0 + \delta\hat{N}, \quad \hat{L} = L_0 + \delta\hat{L} \quad \text{and} \quad \hat{F} = F_0 + \delta\hat{F}.$$

In this case, Montagner & Nataf (1986) present the required expressions for Rayleigh and Love wave phase speeds, which break into contributions from the reference moduli, the perturbation by the effective transversely isotropic (ETI) moduli relative to the reference moduli, and the azimuthally anisotropic (AA) moduli:

$$c_R(T, \psi) = c_0^R(T) + \delta c_R^{ETI}(T) + \delta c_R^{AA}(T, \psi) \quad (\text{A3})$$

$$c_L(T) = c_0^L(T) + \delta c_L^{ETI}(T) \quad (\text{A4})$$

where

$$\delta c_R^{ETI}(T) = \int_0^\infty \left\{ \delta\hat{A} \left. \frac{\partial c_R}{\partial A} \right|_0 + \delta\hat{C} \left. \frac{\partial c_R}{\partial C} \right|_0 + \delta\hat{L} \left. \frac{\partial c_R}{\partial L} \right|_0 + \delta\hat{F} \left. \frac{\partial c_R}{\partial F} \right|_0 \right\} dz \quad (\text{A5})$$

$$\delta c_L^{ETI}(T) = \int_0^\infty \left\{ \delta\hat{N} \left. \frac{\partial c_L}{\partial N} \right|_0 + \delta\hat{L} \left. \frac{\partial c_L}{\partial L} \right|_0 \right\} dz \quad (\text{A6})$$

$$\delta c_R^{AA}(T, \psi) = \int_0^\infty \left\{ (B_c \cos 2\psi + B_s \sin 2\psi) \left. \frac{\partial c_R}{\partial A} \right|_0 + (G_c \cos 2\psi + G_s \sin 2\psi) \left. \frac{\partial c_R}{\partial L} \right|_0 + (H_c \cos 2\psi + H_s \sin 2\psi) \left. \frac{\partial c_R}{\partial F} \right|_0 \right\} dz. \quad (\text{A7})$$

The depth-dependent moduli B_c, B_s, G_c, G_s, H_c and H_s are linear combination of the components of the azimuthally variable part of the elastic modulus matrix in eq. (A2), $\delta C_{\alpha\beta}^{AA}$, as follows: $B_c = (\delta C_{11} - \delta C_{22})/2$, $B_s = \delta C_{16} + \delta C_{26}$, $G_c = (\delta C_{55} - \delta C_{44})/2$, $G_s = \delta C_{54}$, $H_c = (\delta C_{13} - \delta C_{23})/2$ and $H_s = \delta C_{36}$. Note that the azimuthally independent and 2ψ variations in surface wave phase speeds are sensitive only to 13 of the elements of the elastic tensor, and notably only the (1,6), (2,6), (3,6) and (4,5) elements of the elastic tensor outside of the nine elements occupied under transverse isotropy. The other eight elements of the elastic tensor [(1,4), (1,5), (2,4), (2,5), (3,4), (3,5), (4,6), (5,6)] are in the null space of surface wave phase speed measurements.

Montagner & Nataf (1986) present explicit formulas for the partial derivatives in eqs (A5)–(A7) in terms of normal mode eigenfunctions. Instead of using these expressions we recast the problem by computing the partial derivatives numerically which are computed relative to the reference model. The partial derivatives in the expression for the azimuthal term, $\delta c_R^{AA}(T, \psi)$ are equal to the partial derivatives of the azimuthally independent terms [$c_0^R(T), c_0^L(T)$] with respect to the corresponding transversely isotropic parameters (A, C, F, L, N). This feature facilitates the forward computation because the azimuthal dependence of surface wave speeds can be computed using only the partial derivatives with respect to the five elastic parameters of a transversely isotropic medium, which can be achieved using the MINEOS code (Masters *et al.* 2007). Fig. A1 presents the sensitivity of Rayleigh and Love wave phase speeds at 20 s period to perturbations in L, N, C, A and F as a function of depth. Love waves are sensitive almost exclusively to N , being only weakly sensitivity to L , and completely insensitive to C, A or F . In contrast, Rayleigh waves are sensitive to all of the parameters except N .

We represent the depth variation of the moduli by defining each on a discrete set of nodes distributed with depth and linearly interpolating the moduli between each node (Fig. A2). With this approach, we compute the partial derivatives using MINEOS by linear finite differences and convert the integrals to sums in eqs (A5)–(A7). The method is more accurate for Rayleigh than for Love waves and at longer rather than at shorter periods. For example, a constant 10 per cent relative perturbation in the modulus N ($(\hat{N} - N_0)/N_0 = 0.1$, which is 5 per cent in

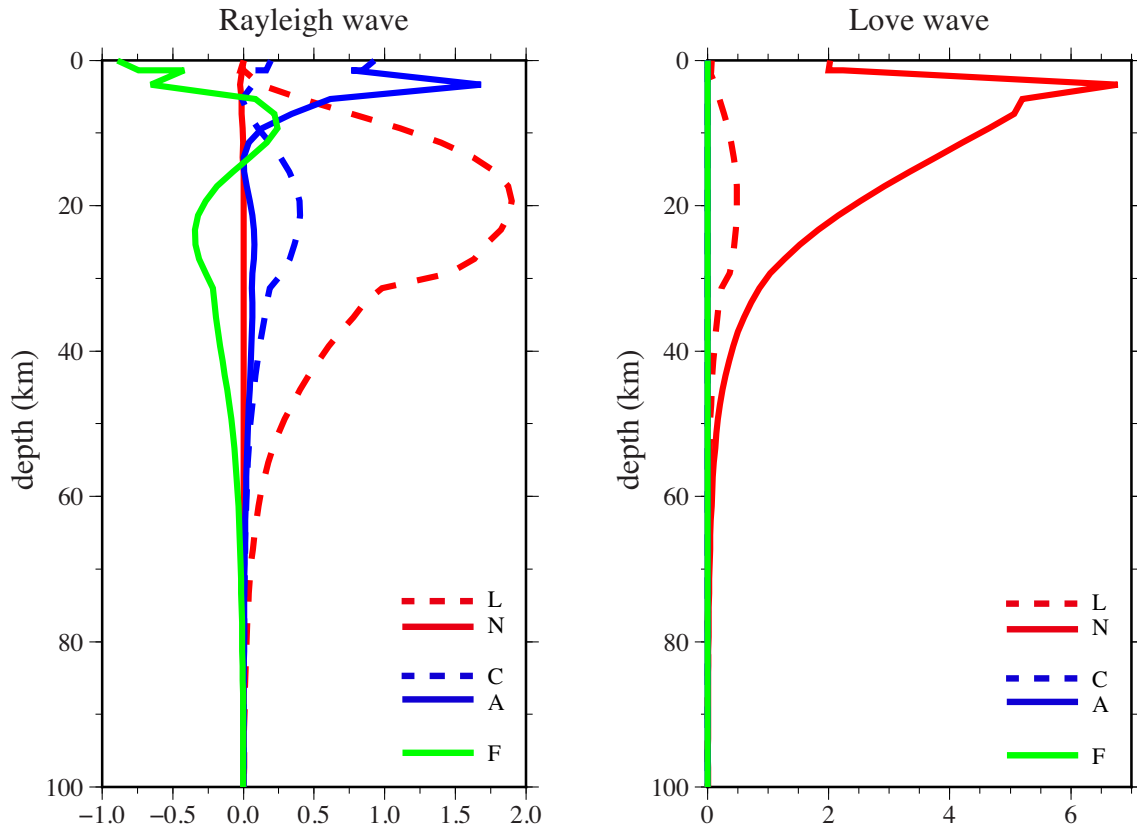


Figure A1. Example sensitivity kernels for Rayleigh and Love wave phase speeds at 20 s period to perturbations in L , N , C , A and F as a function of depth.

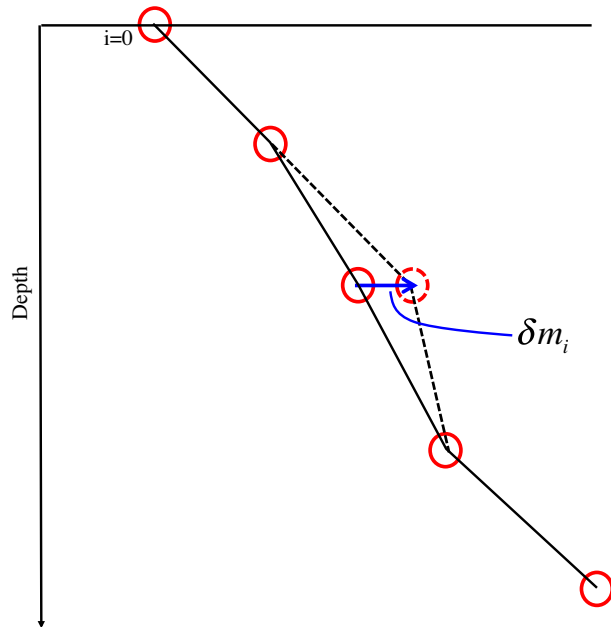


Figure A2. Illustration of the model discretization. At each grid point, the model profile is represented by a vertical set of nodes. Each model parameter is perturbed at each node as shown to compute the depth sensitivity of surface wave data.

V_{SH}) across the entire crust produces an error in the computed Love wave phase speed of less than 0.1 per cent except at periods less than 10 s where it is only slightly larger. For Rayleigh waves, a similar constant 10 per cent perturbation in L ($(\hat{L} - L_0)/L_0 = 0.1$, 5 per cent in V_{SV}) results in an error less than 0.05 per cent at all periods in this study. These errors are more than an order of magnitude smaller than final uncertainties in estimated model variables and, therefore, can be considered negligible.